Characterisation of Silicon Nanoparticles Produced by Mechanical Attrition using Scanning Electron Microscopy, Energy Dispersive X-ray Spectroscopy and X-ray Photoemission Spectroscopy.

David Moweme Unuigbe

A Thesis submitted in fulfilment of the requirements

for the degree of Masters in Science

in the Department of Physics

University of Cape Town

May 24, 2012

Abstract

The establishment of printing technologies, using nanoparticle based inks, promises inexpensive manufacture of electronic devices. However, to produce working devices, nanoparticles have to meet requirements on size, shape, and composition. In the application of silicon nanoparticles in electronics, it is important that a network of interconnecting particles is formed through which charge transport can take place. Of further importance is that there is an absence of surface oxide in order to maintain a direct silicon-silicon connection within the network. In this work, cheap and scalable production of silicon nanoparticles is achieved efficiently with a top-down process of mechanical attrition by high energy milling. Scanning electron microscopy studies reveal that silicon nanoparticles produced by this method have a wide range of shapes and sizes. The shape of the particles tends to become more spherical with milling time as a result of the high attrition rate leading to a high curvature of the particle surface. Compositional studies using energy dispersive X-ray spectroscopy (EDX) and X-ray photoemission spectroscopy (XPS) reveal the impurities present in the milled silicon nanoparticles and their surface properties. The analysis of high energy milled silicon nanoparticles shows that the oxygen contamination during the milling process is low and that the termination of the dangling bonds by oxygen passivates the surface against complete oxidation leading to the formation of stable nanoparticles. These particles are not insulating, but allow charge transport through the surface making them ideal for producing semiconducting nanocomposites particularly for printed electronics.

Acknowledgements

My utmost gratitude goes to the Almighty God for his mercies and faithfulness upon my life. I would like to take this opportunity to thank Prof. D.T. Britton and Prof. M. Härting for their guidiance and assistance. I am grateful to the University of Cape Town, and the Department of Science and Technology, South Africa, for their financial support. I would like to show my gratitude to Mr. Dave Boulton, and Mr. Graham Fowle, both of the Mechanical Workshop, Department of Physics, UCT, and also to Mrs. Miranda Waldron of the Electron Unit, UCT, who were all of help during the course of my research.

To my colleagues, Dr. Ayodele Odo, Dr. Girma Goro Gonfa, Manfred Scriba, Batsirai Magunje, Emmanuel Ohieku Jonah, 'Wole Solana, Stanley Walton, Steven Jones, Sara Abass, Ntombizodwa Mathe, Voarisoa Ramanandraitsiory, Bryce McCall, I say thank you for your assistance and your contribution.

I would like to express my sincere gratitude to my parents, Mr. Ohiomokhai Unuigbe and Mrs. Bose Unuigbe, for their love and continuous support throughout my studies. To my siblings, Ohilebo, Ayodeji, Aifeleoba, Mabel, Airende, and Izevbekhai, I am indeed very grateful for your support. I would like to thank my Angel, Danielle Lungelow for being there for me, you are indeed a blessing in my life. And finally to all my friends and well wishers, I say a big thank you. May the Almighty God reward you all in Jesus name, Amen.

Contents

1. Introduction

Research and development in nanoscience and nanotechnology is fast growing throughout the world because it is anticipated that this field of science will provide the basis for many technological innovations of the 21st century [1]. Nanotechnology involves the simultaneous manipulation of materials on the nanoscale while being able to adapt these materials to form larger and more complex structures. These materials include nanoparticles which play a key role in the development of this field of science [2]. Nanoparticles can be defined as particles with all three dimensions in the order of 100 nm or less. They are presently being investigated for use in different areas such as in electronics [3], biomedicine [4], environmental technology [5], catalysis [6], pharmaceuticals and material sciences [7].

Nanoparticles possess a high surface-to-volume ratio because of their small size. This high surface-to-volume ratio results to an increase in the surface energy of the nanoparticles compared to that of the bulk material [8]. The size effect which includes quantum confinement as well as the high surface-to-volume ratio give nanoparticles different properties from those of the bulk material [9]. Factors which influence these new properties at the nanoscale include not just the size reduction from bulk to nanoscale but also intrinsic properties of the material which become manifested at the nanoscale. Some of these properties include the predominance of surface and interfacial phenomena as well as quantum wave-like transport properties [8] .

The unique properties of silicon and its abundance have been crucial towards the steady growth of the semiconductor industry [10]. On the nanoscale, the electronic and optical properties of silicon are strongly influenced by the shape and size of the nanoparticles. In the case of a collection of nanoparticles, the overall properties are therefore influenced by the size distribution. Varying the production methods of the nanoparticles often varies this distribution [11]. For the synthesis of nanoparticles, many methods have been formulated which includes mechanical attrition, laser ablation, laser pyrolysis and flame synthesis [12]. There is ongoing research on the synthesis methods and physical properties of silicon nanoparticles because of its possible applications in lithium-ion batteries, optoelectronic devices, and photocatalysis [13]. Based on the establishment of printing technologies, there is a lot of prospect towards the fabrication of low cost electronic

devices using silicon nanoparticles.

Silicon has become the most prominent semiconductor material used presently in electronics mainly because of its capacity to form a native oxide [14]. Being an electrical insulator, silicon dioxide can be used for isolation of semiconductor devices, as insulating layers in microelectronics and multichip module technology or as a functional unit in a metal oxide field effect transistor (MOSFET). Hence, controlling the growth of the oxide layer is crucial in maintaining conductivity of the nanoparticles. In contrast, in the application of silicon nanoparticles in printed electronics, it is essential that the particles form a network such that it allows for charge transport within the system [15]. Of further importance is that there is very little or no oxygen present in order to maintain a direct silicon-silicon connection within the network [16].

The aim of this study is to understand the nature of the silicon nanoparticles as a network of particles, produced by milling of bulk silicon with specific application in electronic devices. Of particular interest is the morphology, the elemental composition, and the presence and nature of any oxide layer formed on the nanoparticles during the milling process. This was approached by comparing silicon nanoparticles produced by high energy milling and low energy ball milling using techniques such as scanning electron microscopy (SEM), energy dispersive x-ray spectroscopy (EDX), and x-ray photoemission spectroscopy (XPS). The background of characterisation techniques used in this research is discussed in chapter 3 and is aimed at understanding the fundamental theories underlying the characterisation techniques. The experimental techniques are explained in chapter 4. Chapter 5 covers the experimental procedures which were carried out in this research. The results of the size and shape of the nanoparticles, the elemental composition, and the nature of the oxide layer formed on the nanoparticles are given in chapter 6. The discussion of the results obtained is covered in chapter 7 and the conclusions of the research is covered in chapter 8.

2. Structural Properties and Synthesis of Nanoparticles

2.1 Semiconductor Nanoparticles

Nanoparticles promise to play a crucial role in advancing technologies and therefore, have drawn a lot of interest from the materials science community [17]. Due to their unique physical properties, nanoparticles have potential applications in areas such as photovoltaics, electronics, light-emitting diodes and lasers, and as diagnostic labels in medicine. These applications will require an increasing supply of nanoparticles with well defined properties synthesized by cost-effective and environmental friendly methods [18].

There are two crucial factors which are accountable for the unique properties of nanoparticles. Both factors are related to the size of the respective nanoparticles. The most important in the context of this work is the large surface to volume ratio, but quantum confinement is an important secondary effect [19]. Nanoparticles exhibit new properties different from those of the same material in its bulk form due to structural and electronic changes which are induced by their high surface to volume ratio [20]. Unique photophysical, photochemical, photoelectronic and photocatalytic properties can occur in semiconductor nanoparticle systems [21]. The size, shape and surface features of these nanoparticles determine the properties which they exhibit. For instance, nanoparticles exhibit an increase in the number of available surface specific active sites for chemical reactions as a result of their high surface area to volume ratio [22]. Furthermore, the electronic structure can be altered by the enhanced surface area due to increase in the fraction of surface states relative to bulk levels. However, charge carriers could become confined due to quantum size effect when the size of a particle decreases below the Bohr radius which is a fundamental factor that makes nanoparticles uniquely different from the bulk form of the same material. The quantum effect is crucial in emerging electronic structures such as quantum wires and quantum wells [23].

2.2 Properties and Applications of Nanoparticles

The properties of nanoparticles are largely based on the size of the particle, its shape and surface properties. These properties are dependent on the size and can be classified as either intrinsic or extrinsic. Extrinsic properties, such as resistance, are determined by the size and shape of the material. A list of the modifications to the properties of nanoparticles is given as follows [24]:

- Structural Properties:

  The increase in surface to volume ratio with decreasing particle size results in a higher surface free energy (surface tension) in nanoparticles. In metals, reducing the lattice parameter could lead to a different structure. For instance, silver nanoparticles in the intermediate size range of 5 - 10 nm undergoes a transition from fcc structure to icosahedral structure [25]. In covalent materials such as silicon, the interatomic spacing increases with size reduction [26].

- Thermal Properties:

  The high surface energy and structural changes that occur in nanoparticles influence their thermal properties. As an example, the melting point of gold nanoparticles reduces for particles less than 20 nm [27] but for metallic nanoparticles implanted in a matrix, the melting point can increase [28].

- Chemical Properties:

  The reduction of bulk materials to nanoparticles initiates size effects arising from the considerable increase in the surface to volume ratio. This could lead to a radical change in the chemical reactivity of the nanoparticles. As an example, gold nanoparticles with diameter less than 5 nm is a strong catalyst and is used in the oxidation of carbon monoxide [29].

- Electronic Properties:

  The scarcity of scattering centres with particle size reduction results in ballistic and wavelike transport of electrons in a material. As the system dimension become comparable with the de Broglie wavelength, electronic states become localised with discrete levels, and the materials may become insulators [30].

- Optical Properties:

  The scattering and absorption of light by nanoparticles are very different from that of bulk materials. This is due to the changes in the electronic structure and also the enhancement of surface states. For instance, copper nanoparticles are transparent while bulk copper is opaque. Furthermore, semiconductor nanoparticle elements such as Ge and Si exhibit a blue shift in the optical absorption [31].

2.3 Silicon Nanoparticles

Silicon is of great importance in the field of nanotechnology because there is no variation in composition even at very small scale such as in a nanoparticle and it is an elemental semiconductor [32]. Silicon nanoparticles exhibit unique and excellent size-dependent optical, and electronic properties due to quantum confinement. The size-tunable properties of silicon nanoparticles find wide applications in modern technology such as light emitting diodes [33], quantum dot lasers, solar cells [34], chemical sensors and molecular electronics [35], and printed electronics [36].

For the synthesis of silicon nanoparticles, a lot of methods have been developed [37]. These include gas-evaporation, high-temperature aerosol reactions, electrochemical etching, sputtering, and solid state precipitation after ion implantation [38]. The common disadvantage with these techniques is that the particles cannot be synthesised on a large scale [39]. However, mechanical attrition can easily be used for large scale industrial production of nanoparticles.

2.4 Synthesis of Nanoparticles

As mentioned earlier, there is a wide interest in nanoparticles due to their unusual mechanical, electrical, optical and magnetic properties. As a consequence, a variety of techniques have been established for the synthesis of nanoscale structures and devices. In general, synthesis methods for nanoparticles are typically grouped into top-down and bottom-up approaches, as illustrated in figure (2.1).

In the top down process shown in the figure, a fine powder is formed from the bulk material and then from the fine powder, nanoparticles are obtained. In the bottom up process, atomic clusters or molecules are formed before nanoparticles are produced.

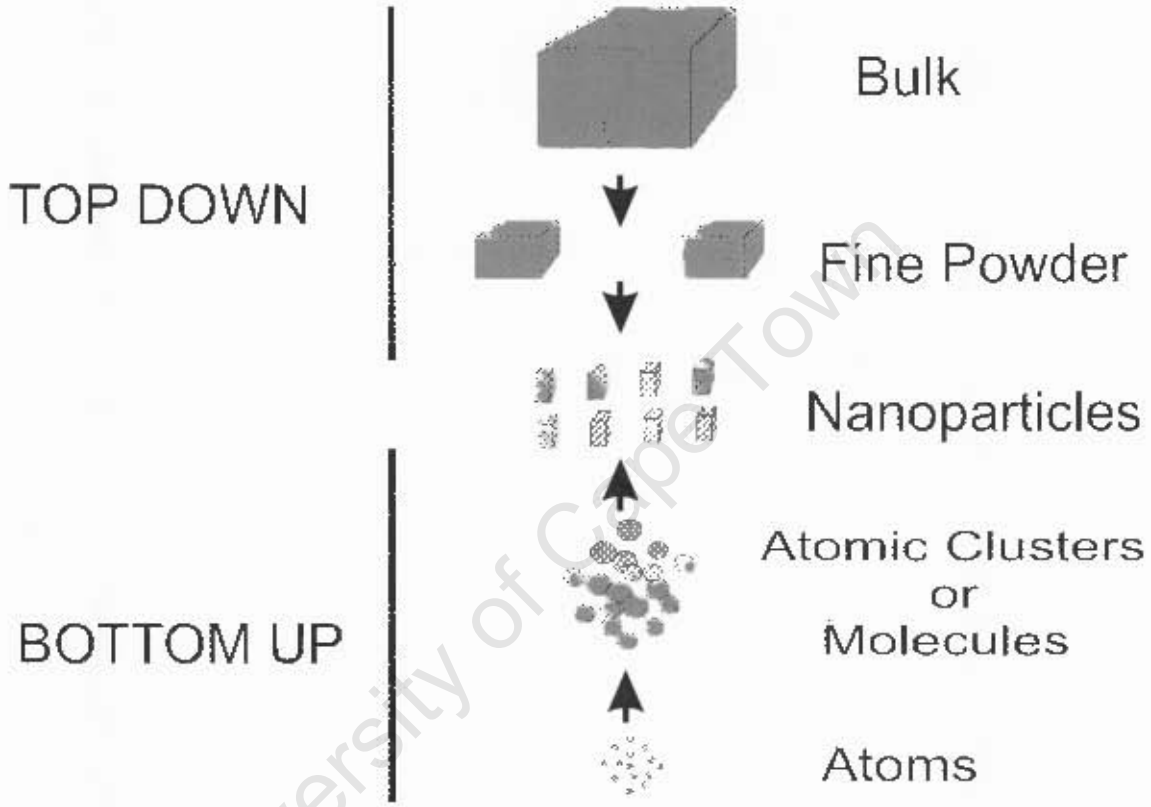

Figure 2.1: Schematic representation of the routes to the formation of nanoparticles [24].

Top down processes for nanoparticle production generally involve the division of a bulk material into smaller portions. The commonly used top down methods include milling, lithographic processes, laser ablation, sputtering, arc plasma, and electron beam evaporation [40]. This approach is very useful in producing nanomaterials in large batches up to industrial quantities due to its simplicity. Many reports on the synthesis of nanoparticles have, on the other hand, indicated that such top-down methods often result in the contamination of the powder, and in the case of high energy mechanical milling, the initiation of strain and defects in the individual particles [41]. The common top down methods used in the production of nanoparticles are:

- Lithographic processes:

  Lithography involves the production of nanoparticles by forming patterns on the surface of a substrate through the creation of a resist [42]. The desired patterns are generated in a suitable mask layer that is subsequently transferred to the underlying layers by etching. It requires the use of electromagnetic radiation such as visible light, ultra violet light and x-rays or charged particles such as electrons and ions to create these patterns.

  In the synthesis of nanoparticles by top-down approaches, there are presently several established and emerging lithographic techniques, such as, photolithography, x-ray lithography, electron beam lithography, ion beam lithography, and nanoimprint lithography [43]. The names of the different lithographic methods are based depending on the approach used to produce the mask.

- Laser induced ablation:

  Laser ablation involves the removing of material from a target surface by intense laser radiation [44]. Monochromatic light is used to remove smaller pieces from the target material to produce nanoparticles. The target could either be ablated in an aqueous solution or in a residual gas. When the target is ablated in an aqueous solution, this leads to the nanoparticles nucleating in the liquid and a colloidal suspension is formed. In contrast, ablation in a low pressure gaseous atmosphere causes nanoparticles to be deposited on a substrate leading to the formation of a nanostructured film [21]. The properties of the synthesized nanoparticles in both cases can be adequately manipulated by the factors of laser ablation.

- Milling:

  In milling, mechanical force is used to break down larger pieces of a material into a large quantity of smaller pieces. In general, reduction in size is due to the repeated distortion of the solid which leads to the mis-orientation of grains within a particle. The ensuing particles are typically fine, irregularly shaped and full of defects such as twins and dislocations [41].

  From a wide range of milling techniques for the production of nanoparticles, high-energy ball milling is considered the most prominent [45]. In general, powders produced by high

energy milling are both nanomaterials, with a particle size distribution less than 100nm, and nanostructured because the individual particles have a grain size between 1 - 10 nm [46]. During the process of milling, unwanted processes such as oxidation are avoided by carrying it out in a controlled atmosphere such as inert atmosphere [41]. The mechanical production of powders can be performed as either the direct size reduction of elemental or compound powders (mechanical milling), or the milling of a mixture of dissimilar powders in which material transfer occurs (mechanical alloying) [47]. Shaker mills, planetory mills, and attritor mills are some popular milling devices used in the production of nanoparticles [46]. The disparities in these milling devices are in their operation, capacity, and efficiency, but the fundamental principle remains the same [46].

In the production of nanoparticles using bottom-up processes, atoms or molecules serve as building blocks [41]. Pure particles synthesized by chemical reaction of a precursor or from inert gas condensation are employed in this process [41]. Common bottom up methods used in the production of nanoparticles are:

- Chemical Vapour Deposition (CVD):

  Chemical vapour deposition (CVD) may be defined as the deposition of a solid film or powder on a heated surface from a chemical reaction in the vapour phase resulting in the nucleation and growth of the nanoparticles [48]. CVD is commonly used for the production of highly pure semiconductor nanoparticles and the method is cost effective [49]. CVD can be categorised according to the type of activation energy employed, namely thermally activated CVD, plasma enhanced CVD, laser induced CVD [50].

  Silicon carbide nanoparticles and silcon nanowires have been fabricated using plasma enhanced CVD [51]. Laser assisted CVD is utilised in synthesizing silicon, silcon carbide [52] and tungsten nanoparticles [53].

  Producing materials in large batches using CVD can be very expensive because of the power and ultra-high vacuum demands of the process, which are responsible for the high costs associated with thin film semiconductor production [54].

- Liquid Phase Methods:

Liquid Phase processes include precipitation, hydrothermal and sol gel methods. These techniques are very appopriate in generating nanoparticles with different shapes since the nucleation, particle growth and the interaction between particles in all stages of the process can be controlled in a liquid medium [55].

This method is not commonly used in the production of nanoparticles due to the fact that clusters produced using this process usually possess poorly defined surfaces and a broad particle size distribution [41].

- Aerosol Synthesis:

  Aerosol synthesis is the formation of liquid or solid nanoparticles suspended in a gas. Several aerosol methods have been reported for the synthesis of nanoparticles [56]. These methods include modified CVD processes as well as gas condensation techniques [57], spray pyrolysis [58], and thermochemical decomposition of metal organic precursors in flame reactors [59].

  Fabricating nanoparticles using the method of aerosol synthesis poses a number of difficulties such as controlling and manipulating nanoparticles after production, in a way the process can be utilised under industrial conditions [60].

In general, nanoparticle production by bottom up processes are employed in the synthesis of highly pure particles with controlled sizes, although a major set-back with these processes is that a large quantity of particles cannot be produced at a time [41].

3. Electron and Photon Interactions in Matter

The analysis methods used in this thesis are based on the spectroscopic analysis of the interactions of electrons and photons with the material under investigation. It is therefore important to understand the fundamental theories underlying the interactions.

Electromagnetic radiation such as x-rays and gamma rays can be described in terms of photons, while correspondingly, particles such as protons, neutrons and electrons can be associated with a wavelength. The de Broglie relationship summarises this wave particle duality of incident radiation [61]:

$$\lambda = \frac{h}{mv}, \tag{3.1}$$

where λ is the de Broglie wavelength of the particle, v is the velocity of the particle, h is Planck's constant and m is the mass. When a beam of light or particles is incident on a material, it can either be absorbed or scattered. A wide range of scattering processes may occur which depend on the type of radiation [24]. A scattering cross section, σ, which gives a measure of the effectiveness of the interaction can be associated with each individual scattering process.

3.1 Electron Interactions with Matter

When a material is bombarded with a beam of electrons, a lot of effects are produced in the target material. After interaction with atoms and electrons of the specimen, the incident beam of electrons are scattered significantly. A schematic representation of electron beam interactions with solid matter is shown in figure (3.1). In general, the electrons are scattered either by elastic or inelastic processes [62].

• In the elastic process, the electron's kinetic energy remains unchanged (no energy transfer) during its interaction with matter, although there may be changes in the direction of the incident wave following scattering due to multiple scattering events. Electrons which escape the sample

are referred to as backscattered electrons and the process is called electron backscattering [63].

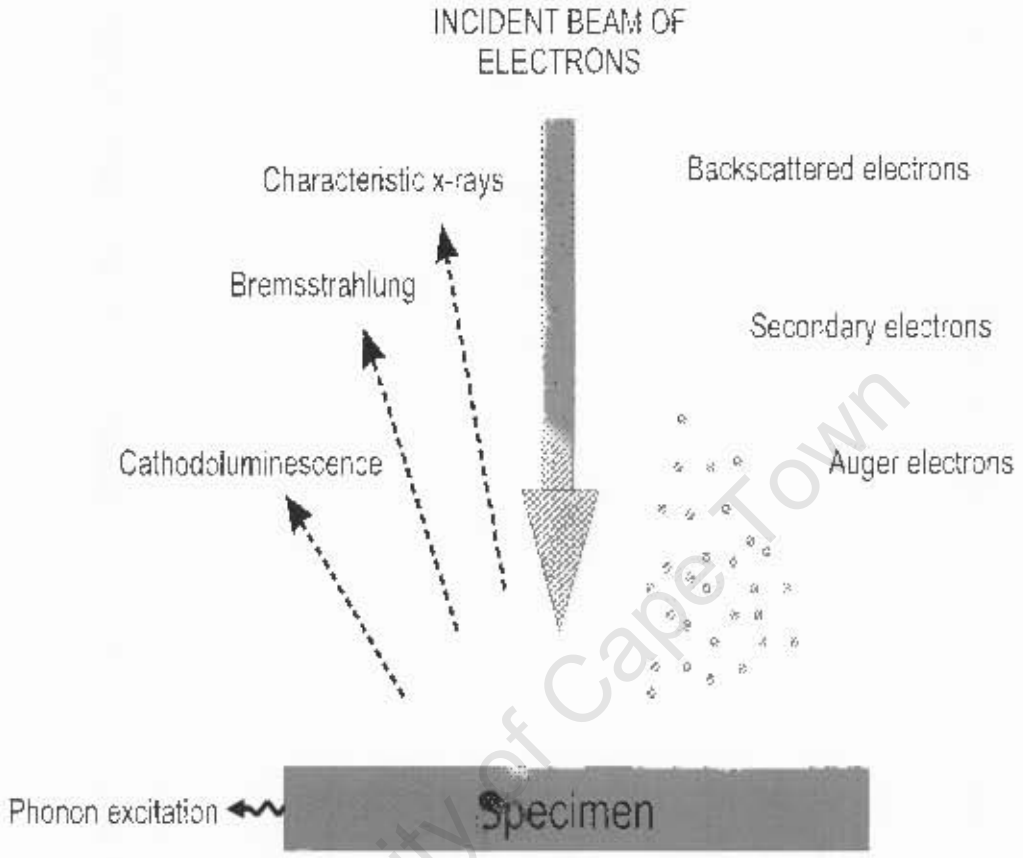

Figure 3.1: Schematic representation of electron beam interactions with a specimen (After [62]).

• In the inelastic process, the incident electrons transfer energy to the atomic electrons after interactions with the specimen [64]. Inelastic scattering yields different effects which includes the following which are discussed below:

- Secondary electron emission
- Bremsstrahlung emission of X-rays
- Atomic excitation leading to:
  - (i) Auger electron emission
  - (ii) X ray emission

(iii) Cathodoluminescence

3.1.1 Backscattered Electrons (BSE)

Backscattered electrons (BSE) are produced when an electron beam interacts elastically with the ion cores in a material. Electrons may be scattered out of the specimen interaction volume, in all directions, with minimal loss of energy. The probability of an electron being backscattered is proportional to the mass of the scattering centre [65]. This implies that higher atomic number elements produce more backscattered electrons than lower atomic number ones. Backscattered electrons may be ejected from a greater depth within the specimen than secondary electrons as they are more energetic [66]. They therefore carry very little topographic information of the sample. They may, however, be employed in identifying variations in chemical compositions of different regions in the sample. The elastic scattering cross section depends on the mass of the scattering centre, and hence the relative brightness of the back scattered electron image increases with the average atomic number in the area of the specimen being probed [67].

3.1.2 Secondary Electron Emission

In practical terms, 'secondary electron' is used to refer to all electrons with kinetic energies less than 50 eV that are ejected from a material [24]. They are produced by the inelastic interactions of an incident beam of electrons with valence and conduction electrons, which cause the ejection of these electrons from the material. Secondary electrons may also undergo additional scattering events within the specimen's interaction volume before some of them emerge from the surface of the material [68]. These emergent electrons are from a couple of nanometres from the surface of the material, and therefore, depending on the position of the detector, provide topographic information of the surface.

3.1.3 Auger Electrons

After an inner shell excitation which can be caused by a collision with a primary electron, an atom has an energy above its ground state. The atom returns to its ground state by filling the empty level created, with an electron from a higher energy level and this leads to the release of energy and momentum. While this energy could lead to an x-ray photon being given off from the atom, it can also be transmitted to another electron leading to this electron's emission [69]. The emitted electron is called an Auger electron and the phenomenom is known as the Auger effect.

3.1.4 X-Ray Emission

Characteristic x-rays are emitted when electrons make transitions between energy levels of an atom [70]. When a material is bombarded with a beam of electrons, electrons can be ejected from inner orbitals and empty levels are created. These are replaced by electrons from higher energy levels, and the excess energy is released in the form of x-rays [71]. Figure (3.2) illustrates this process. An x-ray photon is emitted due to the transition of an orbital electron from a higher energy state to a lower energy state [72]. The change in the binding energies of the associated orbital electrons is equal to the energy of the x-ray photon. These emitted x-ray photons are referred to as characteristic because they are typical of the particular element emitting them and the type of transition that occurs within the atoms of the element. Although, sometimes the excess energy is emitted from the atom as characteristic x-rays, some may be internally absorbed and lead to Auger emission as described above.

These emitted x-rays can be detected and analysed using an energy dispersive x-ray spectrometer. Due to the fact that these x-rays are characteristic of the element producing it, the elemental composition of the sample can be analysed accordingly. Bremsstrahlung emission also occurs when relativistic charged particles are decelerated over a very short distance, such as when the electron beam strikes a solid target [74]. Although usually used in this context, bremsstrahlung actually refers to any radiation given off owing to the acceleration of a charged particle, such as synchrotron radiation emitted by relativistic electrons circulating in a magnetic field [75].

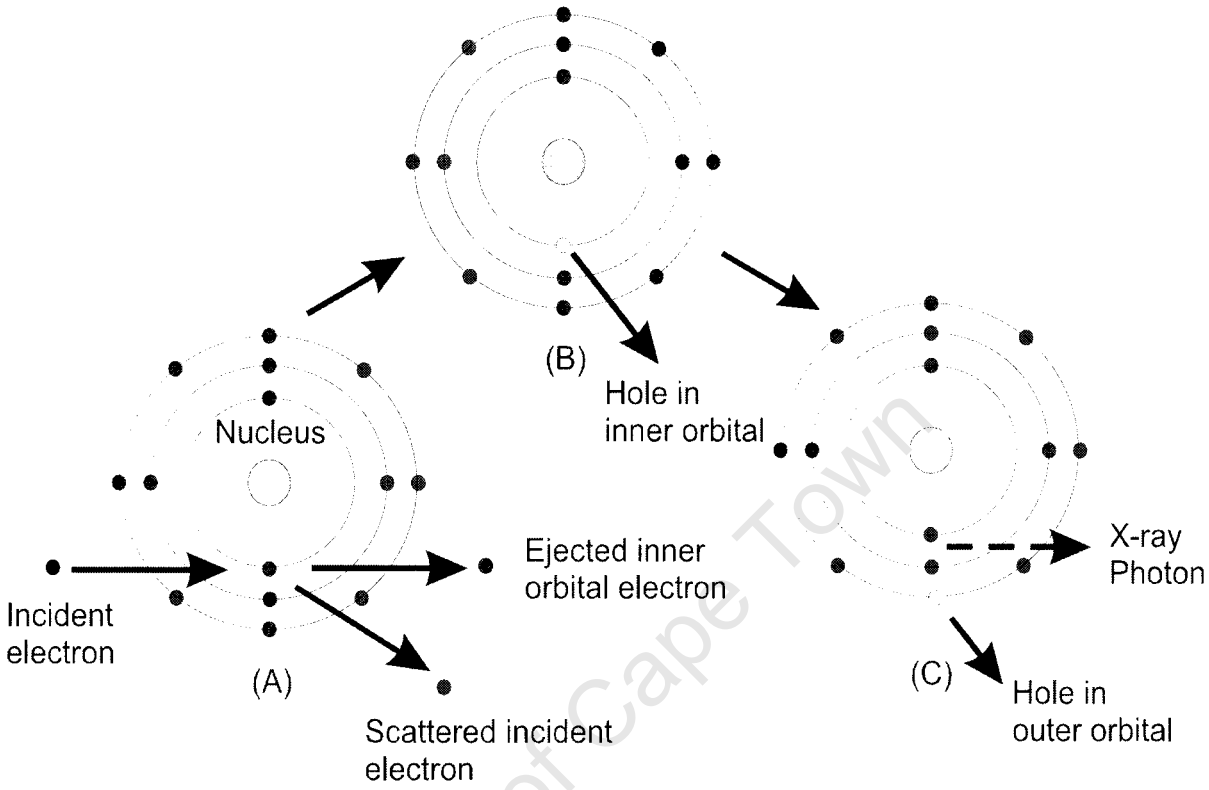

Figure 3.2: Illustration of electron transitions within an atom leading to the emission of characteristic x-ray (After [73])

3.1.5 Cathodoluminescence (CL)

Cathodoluminescence (CL) is the emission of light in the wavelength range 160-2000 nm by materials as a result of electron bombardment [76]. Visible light lies in this regime with wavelengths of about 400 to 800 nm. Wavelengths longer than this are in the infra red region, and shorter than this in the ultra-violet region.

Common forms of cathodoluminescence include the light emission from old fashioned television screens and computer monitors. CL detectors in electron microscopes can either collect the total intensity at different positions or analyse the spectrum of light emitted by the sample [77].

3.2 Photon Interactions with Matter

Interactions of photons with atomic electrons in matter result in either a change of the photon energy or of its direction [78]. The full or partial absorption of the primary photon can lead to the emission of atomic electrons. Photon absorption can be quantified in terms of an absorption coefficient, α, and is a property of a material which defines the amount of light absorbed by it. The light intensity as a function of distance, z, is given by [79]:

$$I(z) = I_0 exp(-(\alpha z)) \tag{3.2}$$

where $I(z)$ is the intensity through a layer of thickness z, and I_0 is the incident intensity on the material.

When a beam of electromagnetic radiation interact with a material, the beam becomes scattered and some of the photons may travel in a different path as the beam. Some photons lose energy to the material while others have the same energy after the interaction as they had before. Such a process results in energy absorption as well as scattering in the medium [80]. The processes of scattering and absorption both results in a reduction in the intensity of the collimated beam.

There are five processes by which a photon can interact with matter [81], whose relative importance depends on the energy of the primary photon:

- Coherent scattering
- Photoelectric effect
- Compton effect
- Photodisintegration
- Pair production

However, only the first three, discussed below, are significant due to the energy ranges in which they occur.

3.2.1 Coherent Scattering

In coherent scatterring, an incident x-ray photon interacts with a target atom and leaves it in an excited state [81]. This leads to a release of energy as shown in figure (3.3). The wavelength and energy of the incident and scattered x-ray photon are essentially the same.

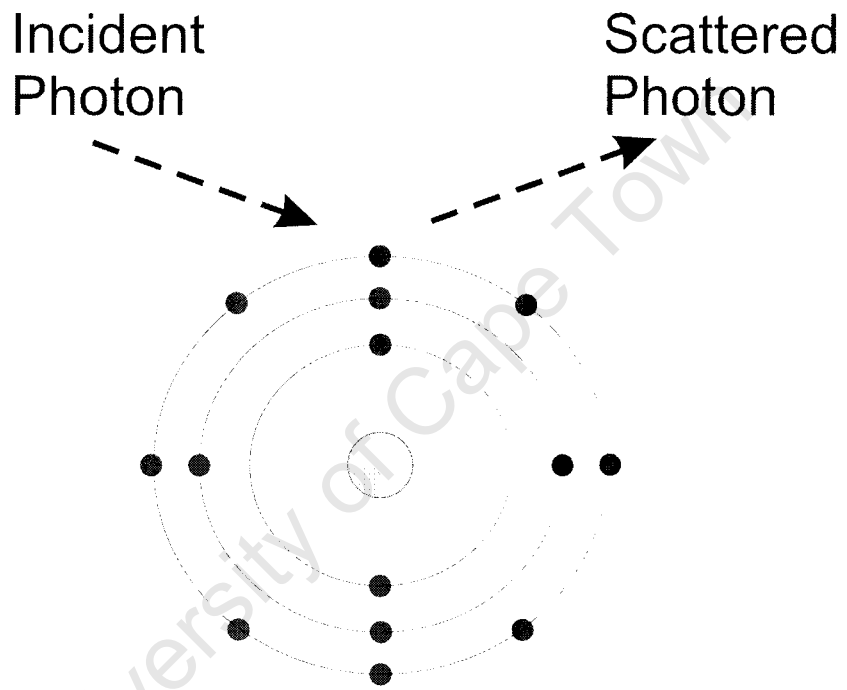

Figure 3.3: Diagram showing the Coherent Scattering (After [81])

3.2.2 Photoelectric Absorption

In the photoelectric absorption process, a previously bound electron called the photoelectron, is ejected from the atom due to absorption of an incident x-ray or gamma ray photon [82]. A schematic representation of the photoelectric absorption process as shown in figure (3.4).

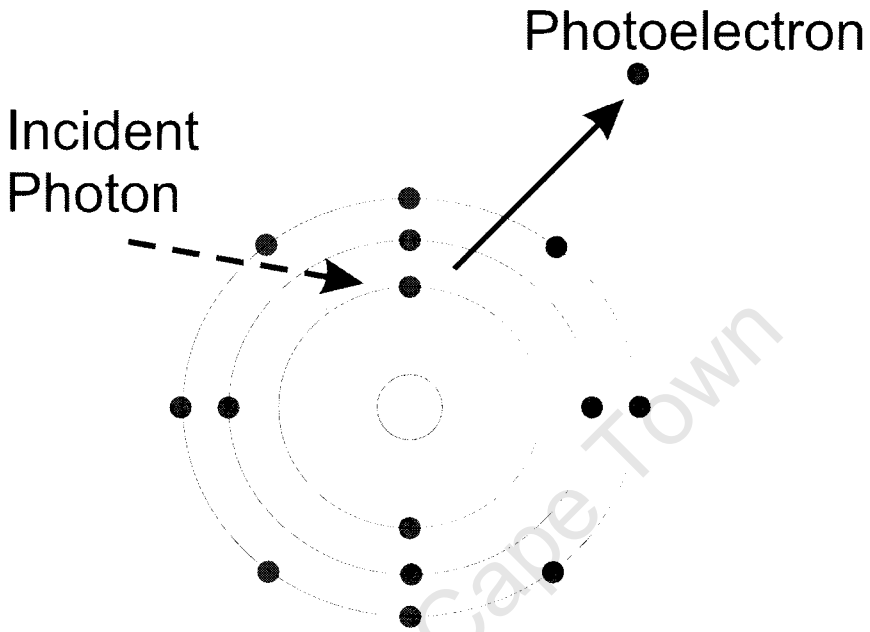

Figure 3.4: Diagram showing the Photoelectric Absorption (After [81])

Relativity and quantum theory are two outstanding ideas in 20th century physics [83]. Although Einstein is renowned for his theory of relativity, he was crucial in the advancement of quantum theory. He proposed that light consisted of discrete quanta, or particles called photons, rather than as continuous waves [84]. For a given frequency, or color of the incident radiation, each photon carried the energy:

$$E_{K_{max}} = h\upsilon - W_0 = \frac{hc}{\lambda} - W_0. \tag{3.3}$$

where h is Planck's constant, W_0 is a characteristic energy associated with a given metal and called the work function, c is the speed of light, and λ is the wavelength.

The photoelectric effect is considered the most convincing proof of the quantization of the electromagnetic field and the restrictions of Maxwell's field equations and hence of the existence

of photons [85].

3.2.3 Compton scattering

Compton scattering occurs when a high energy photon, generally an x-ray or gamma-ray, collides with loosely bound or conduction electrons [86]. The x-ray photon loses energy and momentum due to the collision, and is scattered in a different direction through the material [87]. Figure (3.5) illustrates this process. Additional ionisation interactions with other atoms in the material are possible as both the scattered x-ray photon and the compton electron have sufficient energy to cause these interactions [81]. In the compton process, energy and momentum are conserved. The change in wavelength of the scattered photon is given by [87]:

$$\lambda^{'} - \lambda = \frac{h}{m_e c}(1 - \cos\theta). \tag{3.4}$$

where $\lambda^{'}$ is wavelength of scattered x-ray photon, λ is wavelength of incident x-ray photon, h is Planck's constant, m_e is the mass of an electron at rest, c is the speed of light, and θ the scattering angle of the scattered photon.

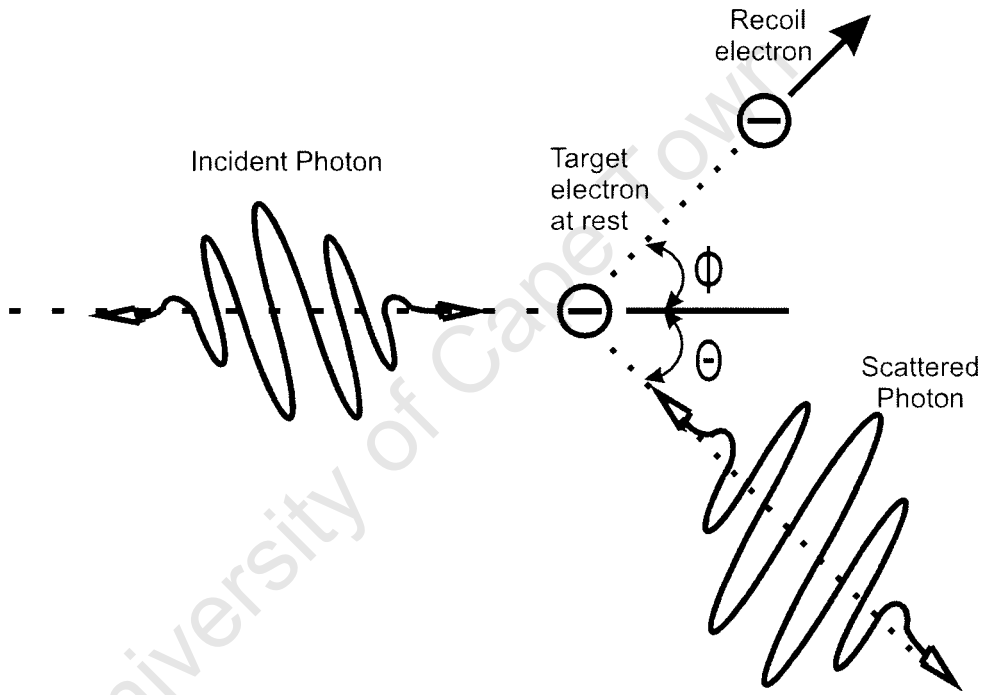

Figure 3.5: Diagram showing the Compton effect where θ is the scattering angle of the photon and ϕ is the scattering angle of the electron (After [81]).

4. Electron Microscopy, Energy Dispersive X-ray Spectroscopy and X-ray Photoemission Spectroscopy

4.1 Electron Microscopy

In all forms of microscopy,the main objective is to obtain a magnified image of an object at the highest achievable resolution [88]. Resolution refers to the minimum separation of points actually observed in the image referred to the size of the object [89]. In an electron microscope, very high resolution of detail in an object is revealed using a beam of electrons [90]. Based on how the image is formed by means of electrons, electron micoscopes are classified as either scanning, transmission or emission. The operation of the first two types involves the interaction of a beam of free electrons with the specimen, while in an emission microscope the source of electrons is the specimen itself. This work is concerned with scanning electron microscopy (SEM). Unlike the other two types which form a direct image, the image is formed by scanning a focussed beam across the sample surface.

In all optics, the Abbé theory is applicable to the mechanisms of image formation and resolution [88]. Abbé was the first to explain on the basis of diffraction effects that there is a limit to the minimum size of an object that can be viewed by a lens and this limit is referred to as the resolving power of the microscope.

The resolving power, R, of any optical system is normally limited by the angular aperture of the objective lens (semi-angle α), and the wavelength, λ, of the radiation employed,

$$R = \frac{0.61\lambda}{n_0 sin\alpha}. \tag{4.1}$$

where n_0 is the refractive index in object space, and the quantity $n_0 sin\alpha$ is usually called the numerical aperture of the lens [91]. It is clear from equation (4.1) that the best resolution will be achieved when the numerical aperture is largest and the wavelength is shortest [92]. Due to

limitations on the values of α, λ, and n_0, the best possible resolution that can be achieved with an optical microscope is about 200 nm [93]. The most significant way to improve resolution is to use radiation with a shorter wavelength since resolution, R, depends on wavelength, λ, as described by the Abbé relation [94]. By using accelerated electrons with an extremely short wavelength, the electron microscope utilizes this principle. The focusing of electrons was demonstrated by Busch in 1926 [95] when he made comparison between light and electron beams, and showed theoretically that a strong short axial magnetic field converged a beam of electrons in a similar manner to which a glass lens converges light.

In 1924, de Broglie suggested that in view of the dual nature of waves and particles, a wavelength, λ, can be attributed with particle beams, such as electron beams. For electrons of mass, m, and velocity, v, the wavelength according to de Broglie is,

$$\lambda = \frac{h}{mv}. \tag{4.2}$$

with h being Planck's constant.

When electrons are accelerated from rest through a potential difference V, their kinetic energy increases to:

$$eV = \frac{1}{2}mv^2. \tag{4.3}$$

where e is the electron charge. From Equation (4.2) for λ, it follows that the relation between wavelength and accelerating voltage is,

$$\lambda = \frac{h}{(2meV)^{\frac{1}{2}}}. \tag{4.4}$$

The relativistic increase in mass should also be taken into account, since for high accelerating potentials the electrons can reach velocities comparable to the speed of light c. This can be easily achieved by substituting V in equation (4.4) with the relativistic accelerating voltage V_r, given by [92]

$$V_r = V[1 + \frac{eV}{2m_0c^2}]. \tag{4.5}$$

where m_0 is the electron rest mass.

4.1.1 Scanning Electron Microscopy

The scanning electron microscope is the most widely used of all electron beam instruments [96]. This is due to the different possible modes of imaging, and the corresponding ease with which the information represented in the micrographs can be interpreted. Figure (4.1) shows a schematic of the principles of a SEM [97]. The measurement signals are secondary electrons, backscattered electrons, characteristic x-rays, Auger electrons, and phonons of various energies.

In a scanning electron microscope, the electron beam is emitted from an electron gun. These electrons are accelerated through an electric potential which can be up to the order of 400 kV [98] but is usually of the order of 5 to 40 kV. This beam of electrons passes through a condenser lens where it is processed into a thin stream of electrons. In the objective lens, two sets of coils that are orthogonal to each other scan a raster on the sample [99]. Secondary electrons are emitted from the sample when the scanned beam of electrons transfer enough kinetic energy to the specimen [100]. These electrons are measured at each point of the scanned region in the specimen using a secondary electron detector. The detector converts the charge pulse to a voltage pulse and amplifies it. In modern microscopes, a computer system converts these voltage pulses into an image in which the intensity of each pixel is dependent on the number of secondary electrons emitted, at the corresponding beam position of the sample.

Electron microscopy has both its pros and cons as compared to light microscopy. Three clear-cut advantages are given as follows [101]:

- A very large depth of field which allows different heights of the sample surface to be in focus at a time. This allows the viewing of irregular surfaces,
- the possibility of a wide range of magnifications, from less than 20× to greater than 100,000×, and
- the ability to obtain information regarding the sample's composition as well as 3D images. Although an electron microscope can produce images that are similar to a light microscope, it can also produce images whose contrast is based on the compositional variation

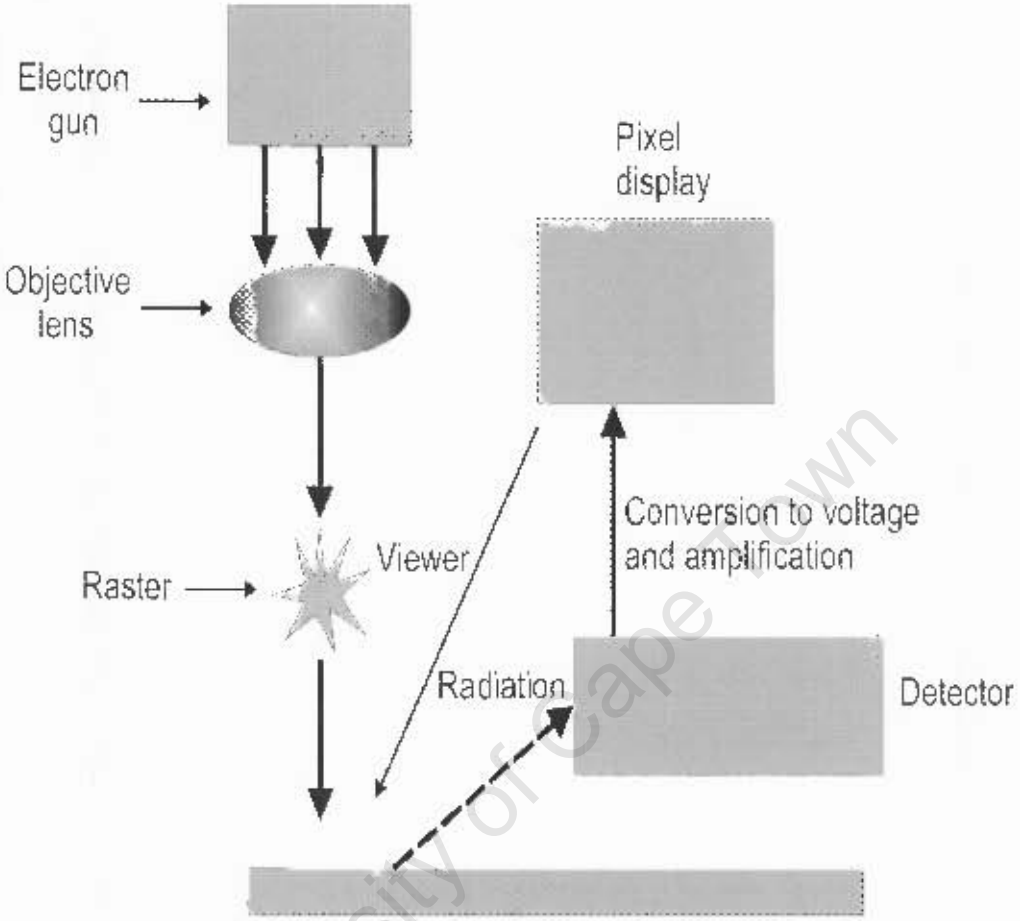

Figure 4.1: Simplified view of a scanning electron microscope (after [97]).

throughout the specimen.

A few drawbacks of SEM are:

- Stability of the specimen under vacuum, and
- In conventional SEM, the specimen must be dry and electrically conductive. Vacuum and conductivity challenges can be reduced by low vacuum electron microscopes and conductive coatings respectively [101].

4.1.2 Energy Dispersive X-ray Spectroscopy

Energy Dispersive X-ray Spectroscopy (EDX) is an analytical technique that is often included in a scanning electron microscope. EDX is used to identify the elemental composition of a sample by detecting characteristic x-ray photons emitted by the atoms near the sample surface after excitation by energetic electrons. In an electron microscope, excitation by electrons has the benefit that they are readily available and the energy, intensity and probe area can be easily controlled [102].

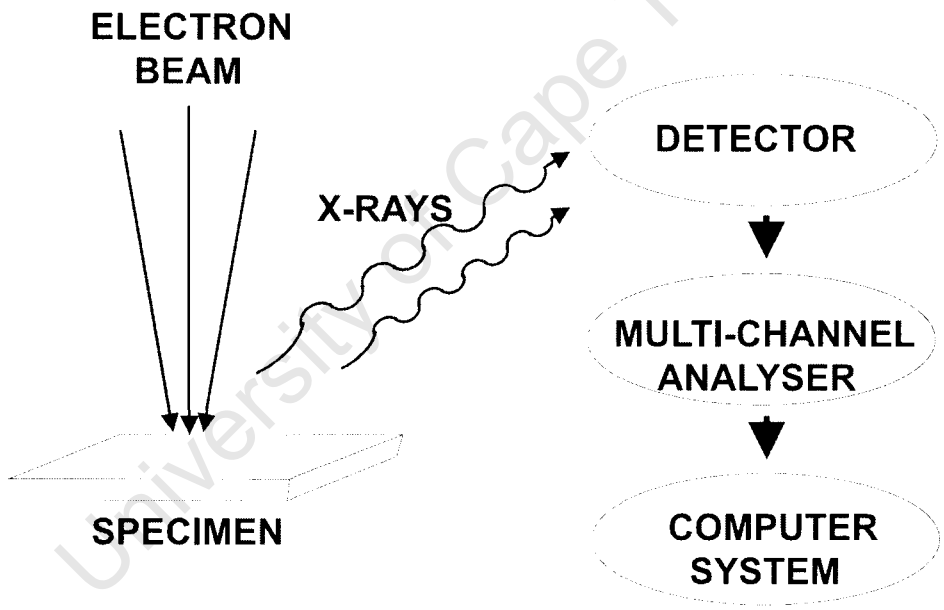

Figure 4.2: A schematic of EDX measurement (after [102]).

The basic elements of an energy dispersive x-ray spectrometer are illustrated in figure (4.2). When a material is irradiated by a beam of energetic electron, electrons may be ejected from the inner shells of atoms close to the surface. The resulting unoccupied atomic state can be filled

by an electron decaying from an outer shell, with an x-ray photon being emitted to balance the energy difference. The x-ray photon is therefore characteristic of the atom from which it was emitted [103]. These x-rays are produced in a region up to about 2 microns below the surface, subject to the energy of the incident electron beam. Because of this high penetration depth, EDX is not strictly a surface science technique [104]. Low atomic number elements which only emit soft x-rays are usually challenging to quantitatively study by EDX as a result of absorption of the emitted radiation in both the detector window and in the sample.

The EDX system measures the intensity and the energy of the x-rays produced in the sample [103]. A lithium-drifted silicon crystal is usually used as the detector in an EDX system. A charge pulse consisting of free electrons and holes is produced when an x-ray photon strikes the detector. The total charge is proportional to the energy of the photon. The pulse is converted to a voltage pulse by a charge sensitive pre-amplifier and sent to a multi-channel pulse height analyzer. By comparing the x-ray energies in the spectrum with known characteristic x-ray energy values, elemental analysis of the sample can be carried out. Elemental mapping can also be carried out in which case the intensity of a particular set of characteristic x-rays is measured relative to the position of the SEM probe on the sample [103].

4.2 X-ray Photoemission Spectroscopy

The theoretical foundation of x-ray photoemission spectroscopy (XPS) was in 1905, when Einstein wrote his well known photoelectric equation [105]:

$$h\nu = E_b + E_K + W_0. \tag{4.6}$$

where $h\nu$ is quantum energy, E_b the binding energy of the electron in matter, E_{Kin} the kinetic energy of the ejected electron and W_0 is the work function of the material. This technique exploits the principle of the photoelectric effect where an electron is emitted from the inner shell of an atom in the sample. The photoelectron spectrum is therefore a measure of the energy levels of the atomic and molecular electron states in the material [106].

The XPS technique offers some very important procedures in the analysis of materials [107].

These include identifying the chemical bonding (ion) environment, and the chemical species in spectra as described below.

XPS is very useful because the energies of the ejected photoelectrons provide information on the bonding state, configuration interactions and the polarization effects of neighbouring atoms [108]. The binding energy is obtained from the difference in the kinetic energy and the energy of the incident photon. Both core and valence electron levels can be identified with XPS, the latter is involved in the chemical bonding and hence sensitive to the local environment of the atom [109].

In x-ray photoemission spectroscopy the two most commonly used sources are aluminium and magnesium [110], with principal K_α line energies 1486 eV and 1253 eV respectively. The kinetic energies of the photoelectrons are therefore in the range 0-1500 eV. X-ray photoelectron spectroscopy is therefore a useful surface sensitive technique due to the limited depth of information which is about 10 nm [111].

4.2.1 Chemical bonding

The core energy levels of atoms in a material are also sensitive to structure and bonding even though they do not actively participate in chemical bonding [112]. Their binding energies are determined by the local electronic structure in the material, and hence chemical shifts provide information about the chemical bonding state of the atoms.

4.2.2 Chemical Species

In the XPS technique, quantitative information on the near surface composition of the specimen can be obtained by the measurement of the intensities of the characteristic photoemission peaks of the different elements in the sample [113]. Since photoelectrons have little energy to penetrate a material, only electrons emitted close to its surface can escape from the material [114]. For this reason, XPS is regarded as a surface sensitive technique capable of revealing information on typical penetration depths of about 5 to 10 nanometers.

5. Experiment and Analysis

5.1 Sample Preparation

Samples were milled by two milling methods:

- High energy milling, and
- low energy ball milling.

The high energy milled samples were milled for different durations and the low energy milled samples were milled by changing the milling media.

5.1.1 High Energy Milling

Nanopowders were produced by high energy milling of bulk 2503 grade silicon in an 800W Siebtechnik laboratory orbital disc pulverizer.

The silicon metal, which had a specified purity of 99.4%, was provided by silicon smelters (pty.) Ltd., Polokawane, South Africa. The main impurities are Fe at 0.21% and Al at 0.144% [115]. Although the Fe and Al impurity levels in the silicon are much higher than the tolerances for standard silicon microelectronics, this silicon has been successfully used in production of working devices [15]. Other impurities specified by the manufacturer were Ca, Ti, Cr, P, and Ni with concentrations, in ppm, of 230, 129, 62, 43, and 18, respectively. The mill has a set of pots or mortars and pestles all of 52100 chrome steel and is shown in figure (5.1). A single pot which is capable of milling up to 50 g of the material in a single milling cycle was used for the silicon.

The metallurgical grade silicon to be milled was weighed using a Vibra AFR220E electronic balance. Powder-free latex gloves were worn to avoid contamination of samples. Furthermore, the pots and pestles were cleaned by first milling a small quantity of silica for a period of 10 mins in order to remove any potential contaminants. The pots were then emptied, cleaned and

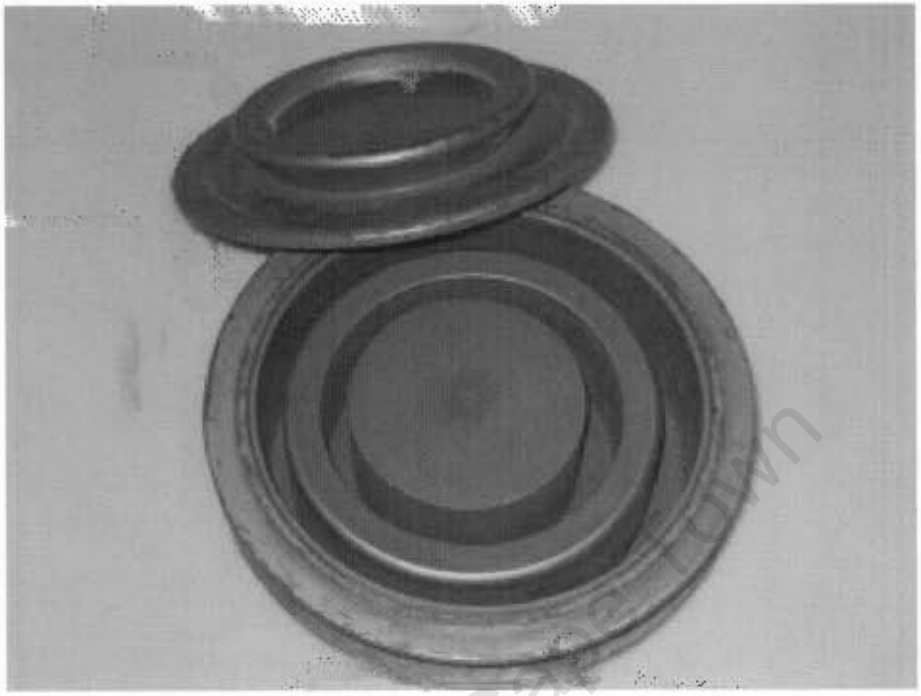

Figure 5.1: Photograph of a single pot milling station containing the ring, pestle and a lid.

rinsed using water, acetone, and then ethanol. At each stage of the cleaning process, the pots and pestles were dried using compressed air to avoid leaving particles in the mortar.

Immediately after cleaning, the weighed silicon was placed in the pot and then covered with its lid. Once this had been done, the pot was then placed in the pulverizer as shown in figure (5.2) and the machine lid closed.

The mill is operated based on an orbital motion of the milling pot. This results in the pestles moving in lateral directions thereby causing the material to grind repeatedly as a result of the impingement of the pestles with the walls of the pot. Milling was carried out in cycles of 30 mins, 1 hour, 2 hours, 3 hours and 5 hours. In order to avoid overheating of the pulveriser, the mill was checked at regular intervals with breaks of 30 mins taken after every hour. Milled powder was retrieved from the pot after it was allowed to cool down at the end of each cycle and was transferred into plastic containers with screw cap lids. The containers were then labelled

Figure 5.2: A photograph showing the interior part of a pulverizer with the pot placed in it.

appropriately and stored under ambient conditions.

5.1.2 Low Energy Ball Milling

For comparison, 2503 metallurgical grade silicon powders produced by low energy ball milling were made available by other members of the group. The milling was carried out in air using two different milling media, zirconia and steel balls. In order to obtain particles in nanoscale, the silicon was milled for a period of 6 weeks. The diameter of the steel balls used was 15 mm while for zirconia 15 mm diameter balls were used for the first week of milling, 10 mm diameter balls for the second week and 5 mm diameter balls for the remaining period.

5.1.3 Pellet Preparation

For characterisation using the scanning electron microscope, pellets were prepared by compaction of powder. This process basically entails two steps: a small quantity (0.25 grams) of silicon nanopowder was placed inside the mould which is shown in figure (5.3). A hydraulic press was then used to apply a pressure of 1 tonne on the mould, thereby compressing the powder into a pellet. The purpose of preparing pellets from nanopowders before characterisation was not only

Figure 5.3: Photograph showing the different components of the mould used to prepare the pellet.

to make it easier to mount the samples in different characterisation equipments, but to prepare uniform surfaces for imaging and analysis using the scanning electron microscope.

5.2 Experimental Methods

In this work, three categories of silicon samples were investigated. The first is the high energy milled silicon which was milled at different durations and are listed as follows:

- 30 mins milled Si,
- 1 hr milled Si,
- 2 hrs milled Si,
- 3 hrs milled Si, and
- 5 hrs milled Si.

The second category is the low energy ball milled silicon samples. These are given as follows:

- zirconia ball milled Si, and
- steel ball milled Si,

which were milled for 43 and 44 days respectively.

The third category is silicon dioxide sample which was obtained in order to compare its known oxygen to silicon ratio with that in the milled Si samples. The silicon dioxide powder was prepared as a pellet and examined under the same conditions as the milled Si samples.

5.2.1 Scanning Electron Microscopy (SEM)

The SEM used in this work is the Leica S440i digital scanning electron microscope as shown in figure (5.4), located at the UCT electron microscope unit which is equipped with an energy dispersive x-ray spectrometer. This was used to study the size distribution and shape as well as the elemental composition of the silicon nanopowders produced above. The pellets were mounted on standard 8mm microscopy stubs using adhesive carbon tape. Because it was intended to perform elemental analysis, the pellets were not coated with carbon or gold. Due to electrostatic charging, silicon dioxide did not produce good images under the SEM. However, it was possible to use the SEM for EDX measurements on SiO_2 as the distorted beam is still able to excite x-rays in the sample volume. The emitted x-rays are unaffected by the electric fields caused by charging of the sample surface. The specimen is held on a stage attached to the door of the chamber. For

imaging, the instrument was normally operated at a beam energy of 20 keV and current of 10 pA using a Lanthanum hexaboride filament. Micrographs were taken using the SEI detector which is used for secondary electron detection. The image quality reduced as the magnification increased thereby making it difficult to locate a primary particle without overlap at higher magnification.

Figure 5.4: A photograph of the Leica S440i digital scanning electron microscope showing: (1) the column and chamber; (2) EDX detector; (3) imaging analysis system; and (4) EDX analysis system.

5.2.2 Energy Dispersive X-ray Spectrometry

The same scanning electron microscope described above, which is equipped with an x-ray detector, was used for elemental compositional analysis of the silicon samples. For this purpose, the microscope was operated at a beam energy of 5 keV and beam current of 1000 pA. When high acceleration potentials are utilised during this measurement, the penetration depth of the incident beam of electrons is increased and this leads to the generation of x-rays deeper in the sample. Low energy x-rays become absorbed when they are generated deeper within the sample. A potential of 5 keV was used in order to overcome this problem of absorption and also to increase sensitivity to the oxygen which is mainly expected to be at the surface. EDX spectra were acquired over 2000 seconds for all milled silicon samples and also for silicon dioxide. Silicon dioxide was used as a standard for comparison because it has a known oxygen to silicon concentration ratio. As mentioned in section 5.2.1, it was not possible to obtain good images of the SiO_2 due to charging of the surface, but this does not affect the EDX measurement. The raw data was exported and analysed with Origin software, to obtain the oxygen to silicon concentration ratio from the relative intensities of the silicon and oxygen $K\alpha$ x-ray peaks in the spectra.

5.2.3 X-ray Photoemission Spectroscopy

The XPS measurements were performed by collaborators at National Metrology Institute of South Africa using a Physical Electronics Instruments (PHI) Quantum 2000 X-ray photoelectron spectrometer with monochromatic Kα radiation and a 100 micron spot size rastered over $0.5 \times 0.5mm^2$, at a take off-angle of 45^0 respectively. The spectral resolution for Al Kα radiation in this specific instrument is not available, but for this model of spectrometer is typically 0.64 eV [116]. The samples were deposited on adhesive coated paper, to give complete coverage. Two different scans were performed on samples: a low resolution scan (broad scan) from 0 to 1.35 KeV at 1 eV per channel; and a high resolution scan at 0.25 eV per channel over a 20 eV range around the silicon 2p photoelectron peak.

The broad scan was used to identify additional contaminants in the milled powders, whereas the high resolution scan was used to study the bonded oxygen in the silicon samples. The silicon

2p peaks were fitted with a superposition of Gaussian functions and an error function for the background as will be described later in chapter 6. There is a shift of the electron binding energy depending on the oxidation state of the silicon [117]. The following conventional notation corresponding to the different oxidation states of silicon was used [118]:

- Si^{0} corresponds to bulk Si, and has a photoelectron emission peak around 98.5 eV as analysed in my spectra.
- Si^{1+} is silicon with one oxygen neighbour, corresponding to a silicon atom in the bulk Si_2O structure, which has an Si 2*p* binding energy shift of 1 eV relative to Si^{0}.
- Si^{2+} is silicon with two oxygen neighbours, corresponding to a silicon atom in the bulk suboxide SiO, and has an energy shift of 1.65 eV.
- Si^{3+} has 3 oxygen neighbours, corresponding to a silicon atom in the bulk Si_2O_3, and has a binding energy shift of 2.5 eV.
- Si^{4+} is fully oxidized Si, corresponding to stoichiometric SiO_2 with an energy shift of 4eV.

6. Results

6.1 Scanning Electron Microscopy (SEM)

In the SLM investigation, the best compromise between feature size and image sharpness (resolution) was obtained at a magnification of 50,000x. Images similar to that shown in figure (6.1) and (6.2), were obtained with the SEI detector using the scanning electron microscope for all high energy milled silicon particles and are included in appendix (A.1.1). The images shown are typical pictures at different positions on the sample surface.

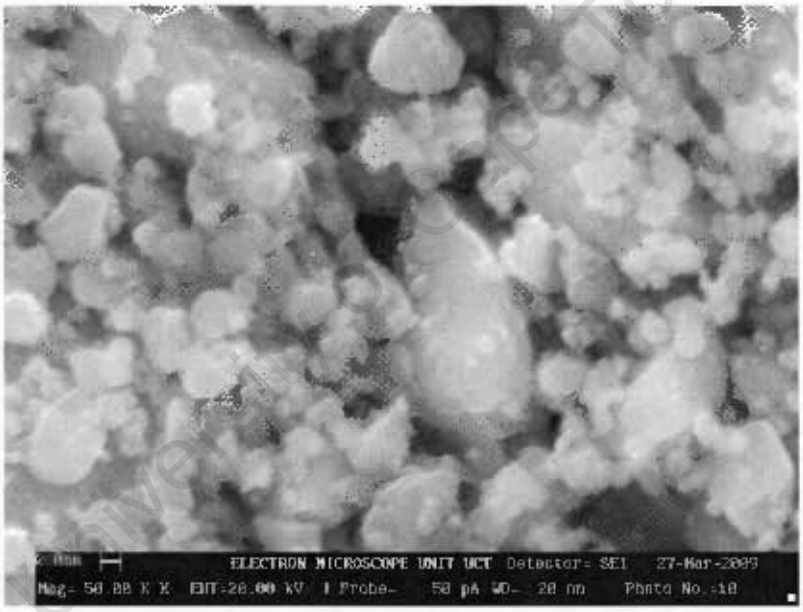

Figure 6.1: A micrograph of the 2503 grade silicon milled for 30 mins.

Figure (6.1) shows that the 30 mins milled Si consists of predominantly small particles, but there are also a few large particles and some clusters. The image also reveals that the large particles are, in general, elongated in shape and the small particles tend to be more spherical. Figure (6.2) is the micrograph for the 5 hr milled Si. The particles are observed to be smaller in size, with larger clusters in comparison to the 30 mins milled particles. Also their shape is spherical.

The micrographs were analysed using ImageJ image processing software [119], to determine

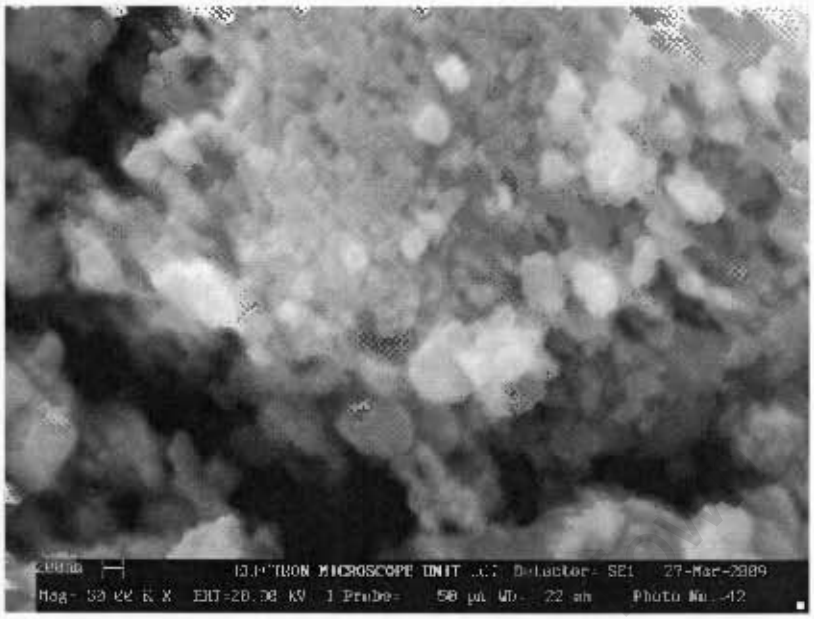

Figure 6.2: A micrograph of the 2503 grade silicon milled for 5 hrs.

the particle size distribution. This was carried out by taking various line scans horizontally and vertically at regular intervals across the image as shown in figure (6.3). The line scan is a measure of the intensity in pixels (brightness) of the image with respect to position. A horizontal line scan of the image is a measure of the intensity in rows of pixels with respect to position, and a vertical line scan gives a measure of columns of pixels with respect to position across the image. Also, the line scans were taken such that they intersected the centre of a number of particles in order to determine the longest segment that cuts across the particles. A total of 50 line scans were carried out, with 20 taken horizontally and 30 taken vertically across each image. In principle, the brighter parts of the image correspond to the particles. A line scan taken for the micrograph of the 30 mins milled Si in figure (6.3) has its corresponding line profile in figure (6.4) which shows a plot of the gray scale (brightness or intensity in pixels) against position (distance).

The widths of the individual peaks were measured from the various line profiles. These widths correspond to the particle sizes. The particle size distribution was then plotted as a histogram, as shown in figure (6.5), using a bin width of 20 nm. This bin width was chosen because it gave a reasonable approximation to the distribution. The distribution is not symmetrical and it has a

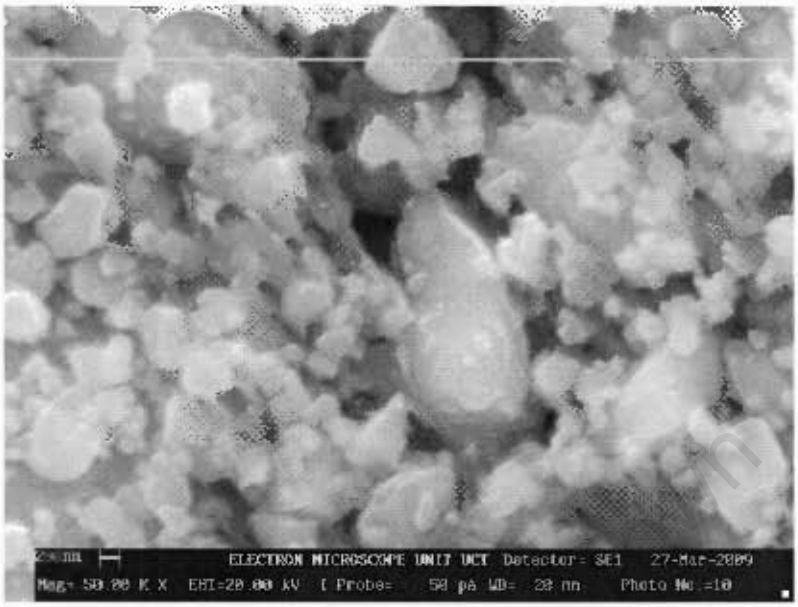

Figure 6.3: A horizontal line scan taken across the micrograph of the 2503 grade silicon milled for 30 mins.

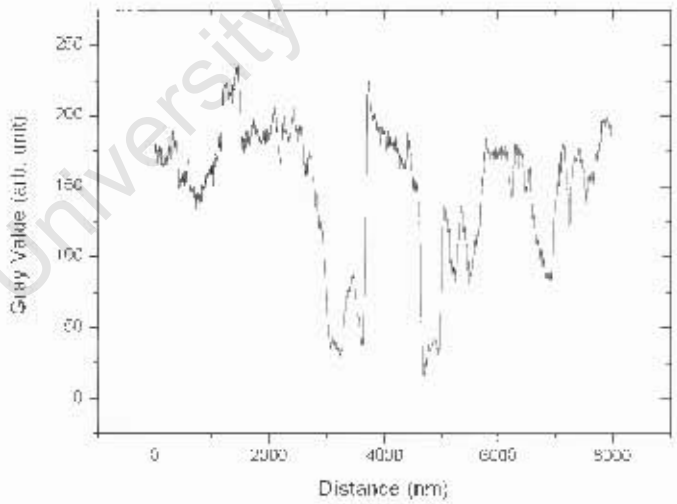

Figure 6.4: A line profile corresponding to the line scan taken across the micrograph of the 2503 grade silicon milled for 30 mins

tail to the larger sizes so it was fitted with a lognormal distribution:

$$y = y_0 + \frac{A}{(\sigma . x\sqrt{2\pi})} . exp(-\frac{\ln(\frac{x}{x_c})^2}{2.\sigma^2}), \tag{6.1}$$

where y_0 is the offset, x_c is the median of the distribution, σ is the logarithmic standard deviation, and A is the area under the curve. The expected value of the particle size, $E(P)$, (mean particle size) is given as [120]:

$$E(P) = exp(\ln x_c + \frac{1}{2}\sigma^2), \tag{6.2}$$

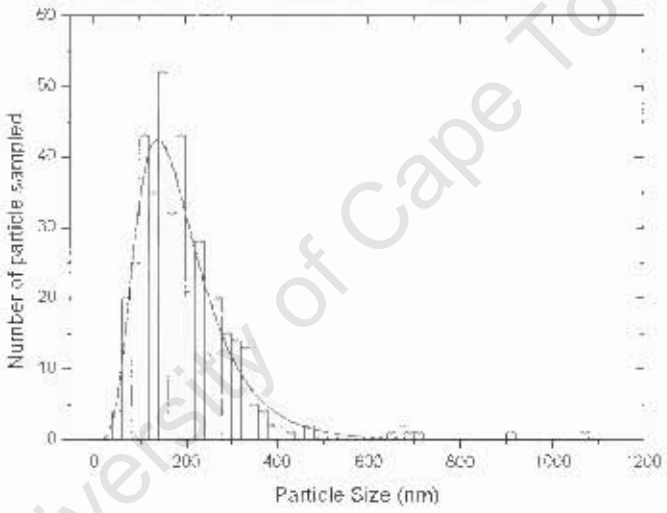

Figure 6.5: Particle size distribution of the silicon milled for 30 mins. The solid line is a lognormal fit with a median of 174 ± 4 nm.

The median particle size, x_c, was found from the fit to be 174 ± 4 nm for the 30 minutes high energy milled, 165 ± 7 nm for 1 hour milled, 157 ± 6 nm for 2 hours milled, 149 ± 3 nm for 3 hours milled, and 112 ± 3 nm for 5 hours milled.

After fitting the particle size distributions with equation (6.1), the logarithmic standard deviation, σ,was obtained. By substituting σ, and x_c, in equation (6.2), the mean particle size, $E(P)$, was calculated and is presented in table (6.1). The errors on the mean particle size are calculated by error propagation from errors on x_c and σ obtained from the fits.

Sample	Median size (nm)	Logarithmic standard deviation σ (nm)	Mean Size (nm)
30 mins milled	174 ± 4	0.48 ± 0.02	195 ± 5
1 hr milled	165 ± 7	0.47 ± 0.04	184 ± 8
2 hrs milled	157 ± 6	0.49 ± 0.04	177 ± 8
3 hrs milled	149 ± 3	0.26 ± 0.01	154 ± 3
5 hrs milled	112 ± 3	0.35 ± 0.02	119 ± 3

Table 6.1: Mean particle size for silicon powder produced by high energy milling for different times.

The variation of the particle size with milling time is shown in figure (6.6). The figure demonstrates that the average particle size decreases continuously with milling time. Although not observed in this work, it is expected that the particle size will reach a minimum value [121, 122] for extended milling times as observed in earlier experiments by Odo [41].

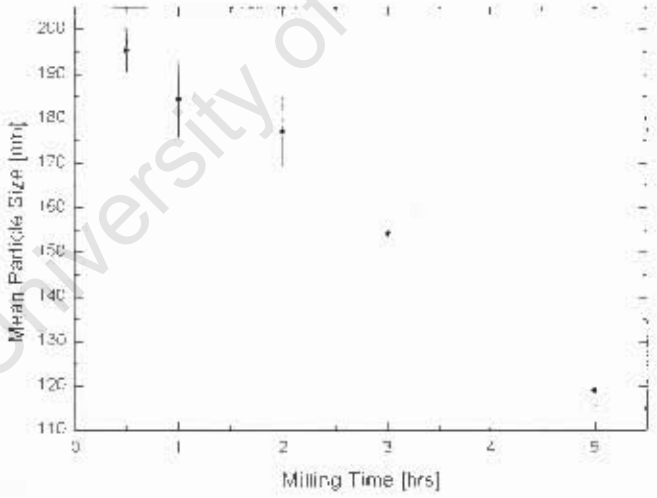

Figure 6.6: The variation of the mean particle size with milling time.

For the low energy ball milled samples, imaging of the particles using SEI on the scanning electron microscope was poor due to electrostatic charging of the samples during electron irradiation. As a result, the particle size distributions for the ball milled samples could not be determined.

6.2 Energy Dispersive X-ray Analysis

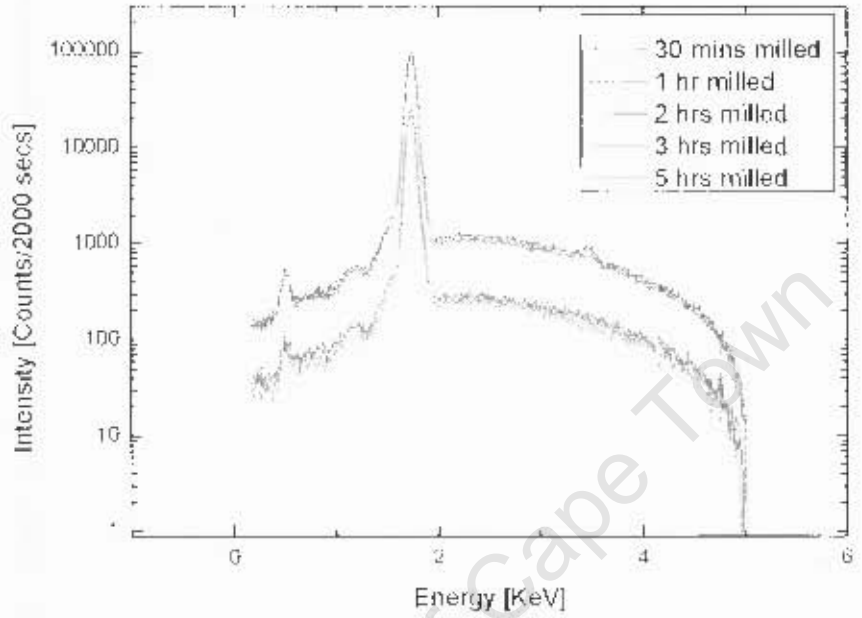

Figure 6.7: EDX Spectra on a semi-logarithmic scale showing the main features of the high energy milled silicon samples. The absolute intensity of the spectra for 30 mins and 1 hr milled Si is lower because of a large sample-detector distance.

The plots of intensity versus x-ray energy obtained from experimental data for all the high energy milled silicon samples are shown in figure (6.7). The background of the spectra has an approximate Gaussian shape because at lower energies, low energy photons are absorbed in the sample and detector window, and at higher energies, the probability of exciting a photon is low. During measurement, the stage position was further away from the detector for the 30 mins, 1 hr milled, SiO_2 and ball milled Si samples in comparison to the 2 hr, 3 hr and 5 hr milled Si samples. Hence, a lower absolute intensity is observed for their spectra. A similar effect is seen in the spectra for SiO_2 sample and ball milled samples. The main features of the spectra are the carbon, oxygen and silicon $K\alpha$ peaks. Additional peaks at 0.67 KeV, 1.49 KeV, and 3.59 KeV seen in some of the spectra can be attributed to iron $L\alpha$, aluminium $K\alpha$, and calcium $K\alpha$ impurities in the silicon.

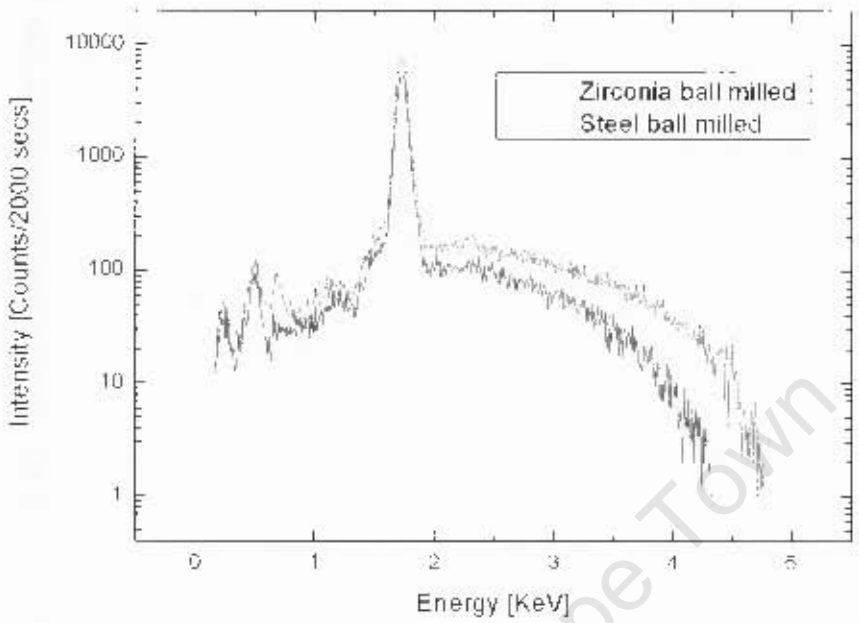

Figure 6.8: EDX Spectra on a semi logarithmic scale showing the main features of the low energy milled silicon samples.

In the case of the low energy milled 2503 grade silicon samples as shown in figure (6.8), the spectra show additional peaks in comparison to the spectra for the high energy milled samples. The main features of the scan are peaks attributable to carbon, oxygen, silicon, aluminium, germanium and iron. For the steel ball milled sample, the iron $L\alpha$ peak is more visible indicating contamination from the milling media. In all the spectra, a peak appears at 1.186 KeV, which corresponds to Ge $L\alpha$ [123].

In order to accurately fit all the data, the spectra were fitted with a superposition of Gaussian functions corresponding to the number of peaks in each sample and an error function for the background. Particular interest in fitting the data was paid to the oxygen and silicon peaks so as to acurately determine the oxygen to silicon concentration ratio in the samples.

Figures (6.9), (6.10) and (6.11) show the plots of the x ray intensity versus energy for the low energy zirconia ball milled, 5 hr high energy milled and silicon dioxide samples. Other plots are included in appendix (A.2.1).

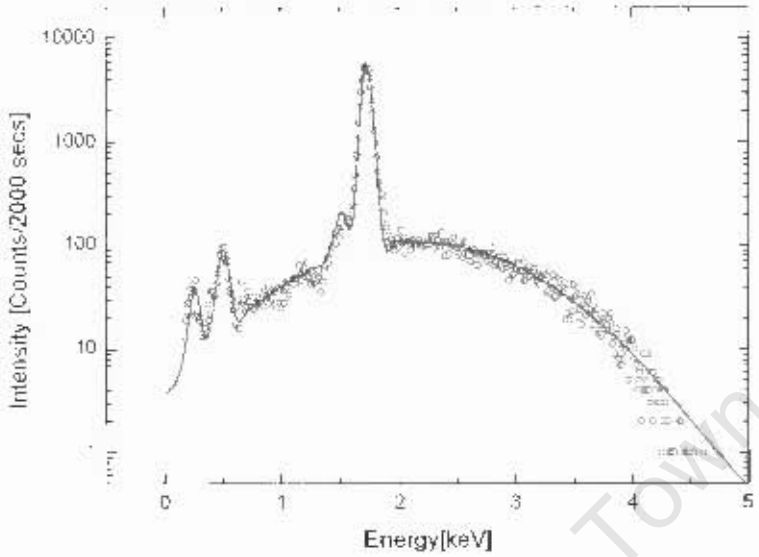

Figure 6.9: Energy dispersive X-ray spectra of zirconia ball milled silicon. The solid line is a least squares fit to the data.

The spectra were fitted with a superposition of Gaussian functions i.e mainly for the oxygen peak which occurs at $K\alpha = 0.525KeV$, the silicon peak at $K\alpha = 1.739KeV$ and for the background. The oxygen to silicon concentration ratio in the samples were determined from their respective fitted spectrum by comparing the ratio of the oxygen peak intensity to silicon peak intensity for each spectrum to the same ratio in silicon dioxide and is shown in table (6.2).

The reference material (silicon dioxode) is a stoichiometric oxide and measurements carried out for different samples of the reference material show similar spectra under different conditions. Hence, it is expected that the oxygen to silicon ratio is uniform over the range of analytical conditions employed.

From the reference spectrum of silicon dioxide, shown in figure (6.11), the oxygen to silicon concentration ratio in all samples was calculated using equation (6.3) by comparing the ratio of the oxygen peak intensity to silicon peak intensity. The oxygen to silicon ratio, R_{os}, in the silicon samples is given as:

$$R_{os} = \frac{1}{K}\frac{I_O(Si)}{I_{Si}(Si)}, \tag{6.3}$$

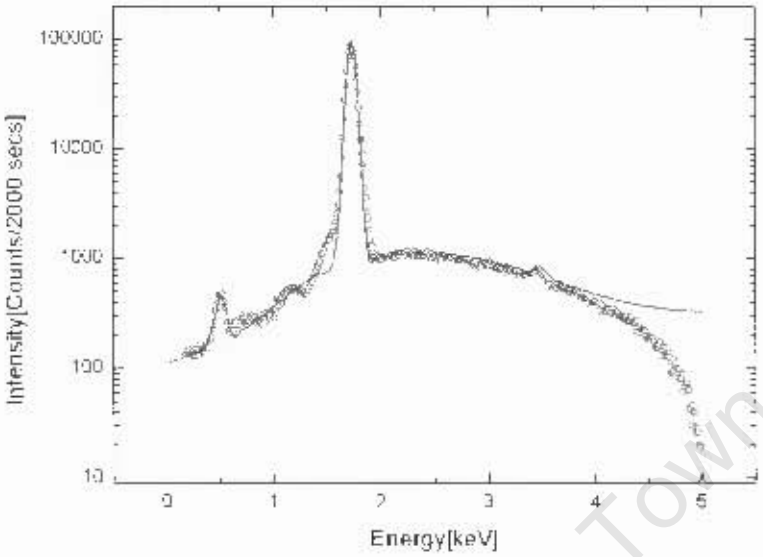

Figure 6.10: Energy dispersive X-ray spectra of 2503 grade silicon milled for 5 hrs. The solid line is a least squares fit to the data.

where I_O is the intensity of oxygen, I_{Si} is the intensity of silicon. From the measurement of SiO_2, the calibration constant, K, can be determined from:

$$K = 2\frac{I_{Si}(SiO_2)}{I_O(SiO_2)}, \tag{6.4}$$

where the factor of 2 accounts for the known atomic ratio of oxygen to silicon. The SiO_2 powder has similar density and surface topography to the silicon samples therefore differences in absorption can be neglected. However, it should be noted that the oxygen concentration may be overestimated if there is significant contamination with Cr from the milling media, because of contribution to the estimated oxygen $K\alpha$ intensity from Cr $L\alpha$ x-rays at a similar energy.

The calculated oxygen ratios in the milled samples are presented in table (6.2).

The high energy milled samples have a fairly constant oxygen ratio with an average value of $8.4 \pm 1.7\%$. For the ball milled samples the oxygen ratio is considerably higher suggesting the presence of a thick oxide layer.

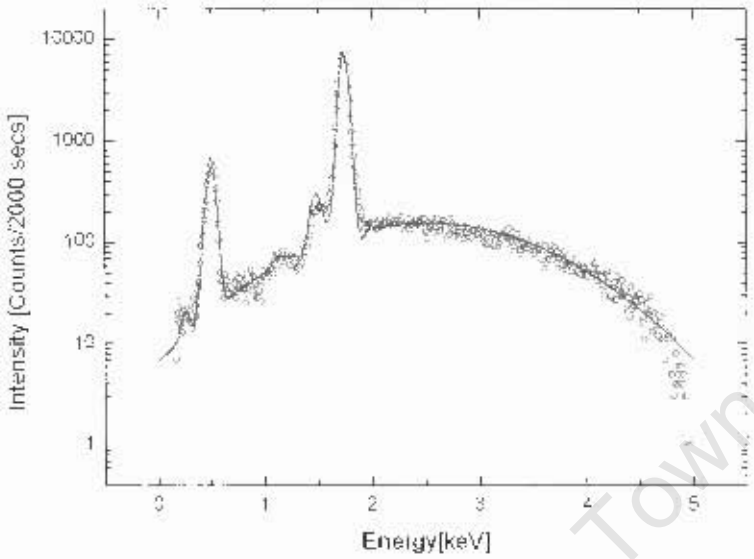

Figure 6.11: Energy dispersive X-ray spectra of Silicon dioxide. The solid line is a least squares fit to the data.

	Sample	Ratio of Oxygen to Si, R_{os} (%)
High Energy milled	30 mins milled silicon	$6.7 = 1.2$
	1 hr milled	$5.8 = 1.5$
	2 hrs milled	$9.7 = 1.7$
	3 hrs milled	$11.0 = 2.2$
	5 hrs milled	$8.6 + 1.8$
Low Energy milled	Steel ball milled	$35 = 3.1$
	Zirconia ball milled	$38 : 3.2$

Table 6.2: The oxygen to silicon concentration ratio in the milled silicon samples.

6.3 X-ray Photoemission Spectroscopy

Plots of photoemission intensity versus the binding energy were derived from a quantitative analysis performed in this work for low and high resolution scans from experimental data obtained from XPS experiments carried out by collaborators at NMISA.

Broad scan XPS spectra for the 5hr milled, 43 day zirconia milled and 44 day steel ball milled are shown in figure (6.12). The main features in all the spectra are due to oxygen (O $2p$ peak at 7 eV, O $2s$ peak at 23.1 eV, O $1s$ peak at 531.8 eV, and O *kll* peak at 979.7 eV), Carbon (C $1s$ peak at 285.0 eV, and C *kll* peak at 1221.4 eV) and silicon (Si $2p$ peak at 99.8 eV, and Si $2s$ peak at 150.5 eV). The Fe $3p$ peak is visible in the spectrum for steel ball milled silicon at 52.6 eV.

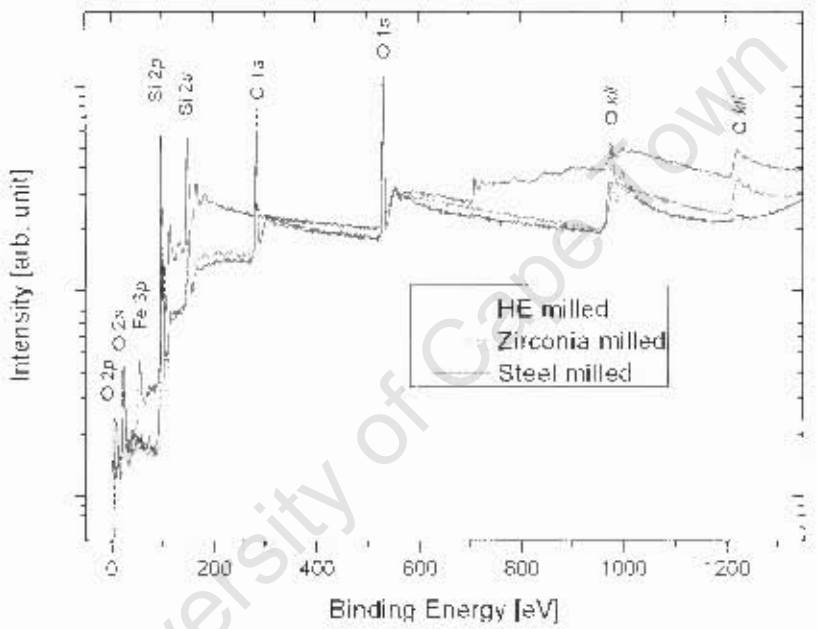

Figure 6.12: Broad scan XPS spectra normalised to the same scale for clarity showing the main features.

An expanded plot of figure (6.12) is shown in figure (6.13). Fe $2p$ peaks and the Fe *lmm* edge are noticed at 711 and 725 eV and between 780 and 890 eV for the steel ball milled Si, indicating contamination from the milling media.

Figures (6.14), (6.15) and (6.16) shows the high resolution scan of Si $2p$ photoelectron peaks for the zirconia ball milled, steel ball milled and high energy milled samples. Similar plots were obtained for other samples and are included in appendix (A.2.2). Plots were fitted with a superposition of Gaussians corresponding to the photoemission peaks of the different Si oxidation

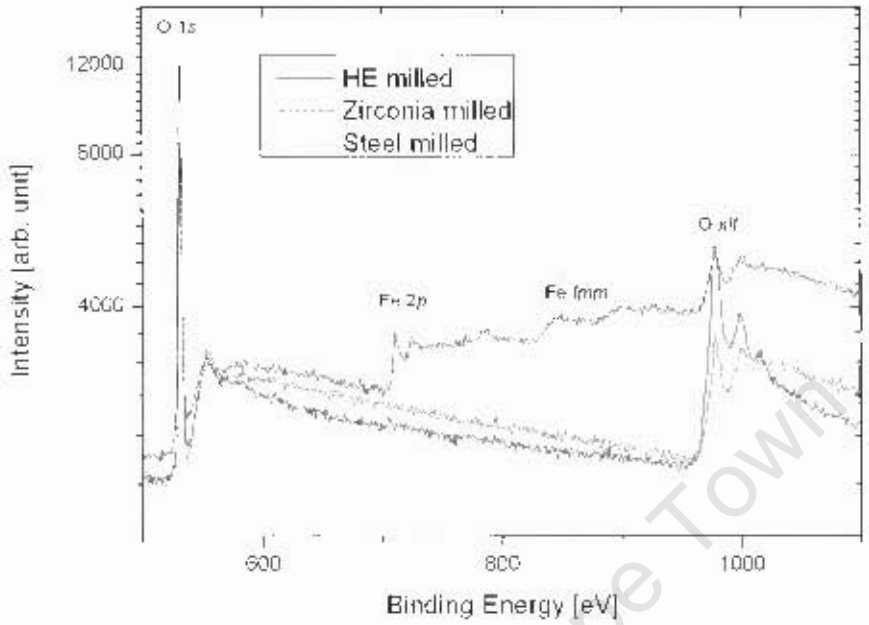

Figure 6.13: Broad scan XPS spectra in the region of the Fe 2*p* photoelectron peak and *lmm* emission edges.

states. The plots are dominated by two peaks, which correspond to the Si^{0} and Si^{4+} states, but in all spectra, at least one extra component due to an immediate oxidation state was required. The relative intensity of each state was determined from the intensities (areas) of the Gaussian components with the peaks having a full width half maximum of 1. Table (6.3) gives the fit results of energy and intensities of the peaks for suboxides in the milled silicon. Also, an error function background was added in the numerical model.

The spectrum for the zirconia ball milled sample has an additional component mainly 1.5 eV above the emission line of bulk silicon corresponding to Si^{2+}, and the spectrum for the steel ball milled sample has a component 1 eV above the emission line of bulk silicon corresponding to Si^{1+}. In both ball milled samples, the intensity of the Si^{1-} oxidation state is higher than the Si^{1+} state.

In high energy milled silicon, the intensity of the 4− state is much lower relative to the 0 state than for the ball milled samples. The high energy milled samples have components mainly 1

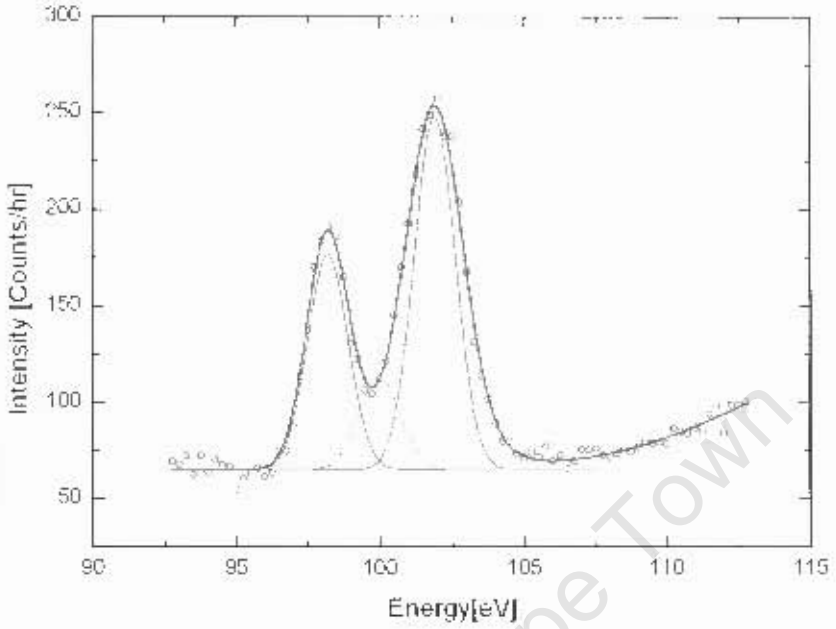

Figure 6.14: Si 2*p* photoelectron peaks for Si ball milled with zirconia media for 43 days. The solid line is a fit to the data as described in the text.

eV and 1.5 eV above the energy of Si^0, corresponding to Si^{1+},Si^{2+}. Figure (6.17) shows the intensities of the different Si 2p components as a function of time of the high energy milled Si. The Si^{1+},Si^{2+} intensity has a large uncertainty relative to its low intensity since no separate peaks are resolved.

The figure demonstrates that the intensities of the Si^{4+} oxidation state is constant with increasing milling time. Also, the intensity of the Si^{1+},Si^{2+} component does not show any systematic variation with respect to milling time.

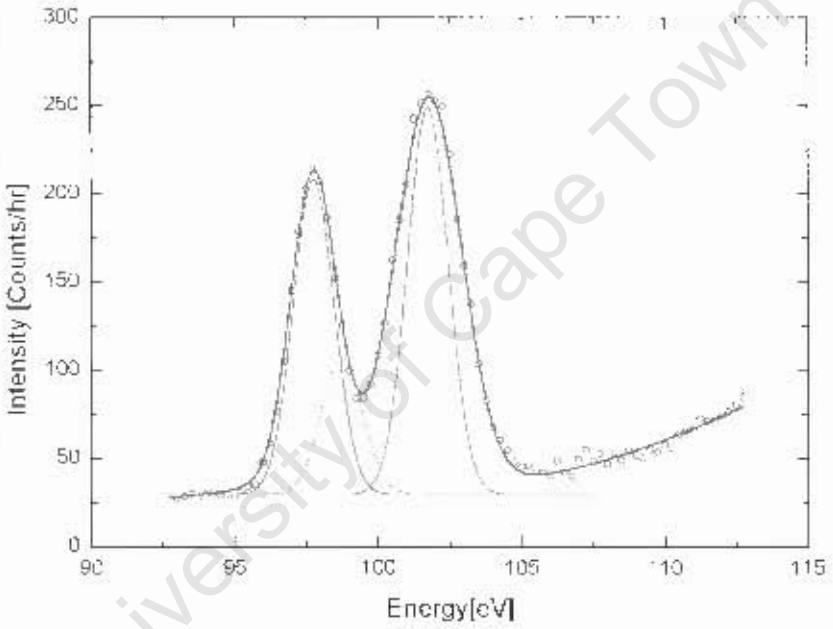

Figure 6.15: Si 2*p* photoelectron peaks for Si ball milled with steel media for 44 days. The solid line is a fit to the data.

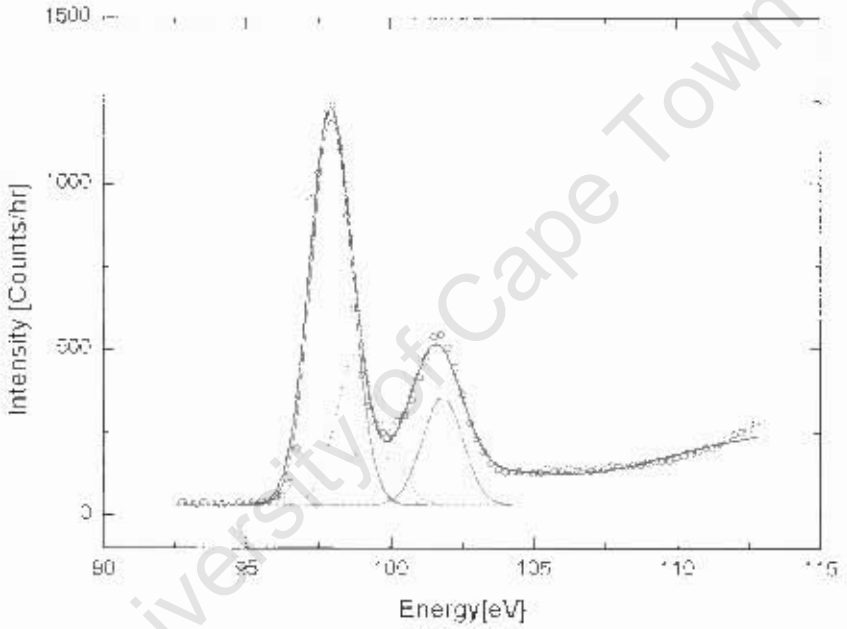

Figure 6.16: Si $2p$ photoelectron peaks for Si milled for 5 hrs by high energy milling. The solid line is a fit to the data.

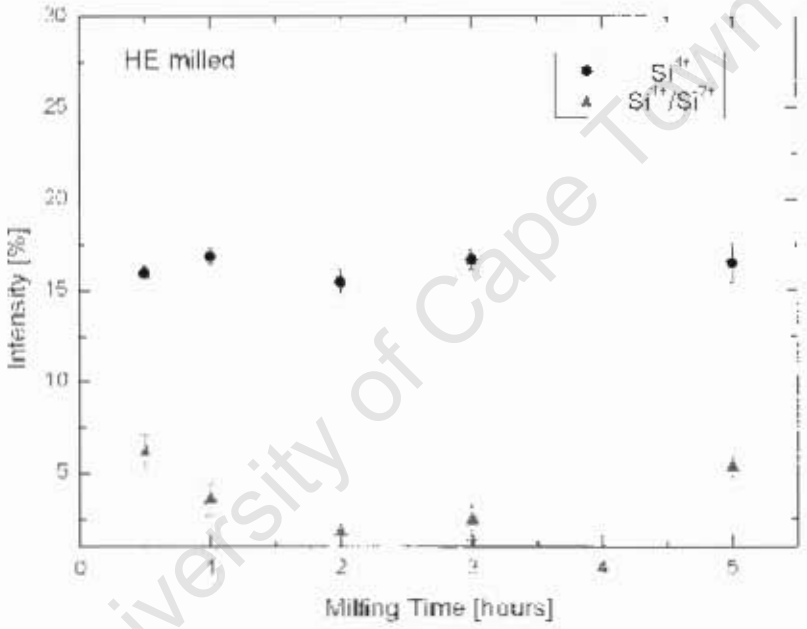

Figure 6.17: Intensity of the photoelectron peaks of different Si oxidation states as a function of milling time for the high energy milled samples.

		Si^0	Si^{1+}	Si^{2+}	Si^{4+}
30 mins milled	Energy(eV)	97.75 ± 0.24	98.46 ± 0.13	99.29 ± 0.72	101.50 ± 0.61
	Intensity(au)	2042 ± 324	1183 ± 437	395 ± 187	607 ± 48
1 hr milled	Energy(eV)	97.52 ± 0.38	98.22 ± 0.68	99.02 ± 0.54	101.50 ± 0.49
	Intensity(au)	1315 ± 245	845 ± 311	378 ± 76	439 ± 53
2 hrs milled	Energy(eV)	98.05 ± 0.71	98.75 ± 0.76	99.25 ± 0.61	101.75 ± 1.72
	Intensity(au)	2138 ± 124	898 ± 571	514 ± 96	601 ± 73
3 hr milled	Energy(eV)	97.75 ± 0.69	98.75 ± 0.17	99.25 ± 0.72	101.75 ± 0.81
	Intensity(au)	2098 ± 128	809 ± 472	523 ± 82	594 ± 54
5 hrs milled	Energy(eV)	97.75 ± 0.38	98.75 ± 1.69	99.25 ± 0.82	101.75 ± 0.79
	Intensity(au)	2076 ± 201	812 ± 563	461 ± 195	579 ± 67
Zirconia ball milled	Energy(eV)	98.20 ± 0.96	-	99.97 ± 0.67	101.90 ± 1.21
	Intensity(au)	198 ± 21	-	86 ± 41	327 ± 36
Steel ball milled	Energy(eV)	97.76 ± 0.58	98.74 ± 0.45	-	101.73 ± 0.93
	Intensity(au)	318 ± 25	139 ± 52	-	391 ± 41

Table 6.3: Energy and intensity of fitted suboxide peaks in the milled silicon samples.

7. Discussion

The size, shape, and composition of the silicon nanoparticles milled for different durations has been investigated using scanning electron microscopy, energy dispersive x-ray spectroscopy and x-ray photoemission spectroscopy. The SEM images show particles with a wide range of sizes, most of which are approximately spherical in shape, but there are also relatively few irregularly shaped large particles or clusters. The distribution of the sizes extracted from these images also shows that the particle size is predominantly small with there being a few large particles. As there is a tail to the larger sizes, the size distributions are well represented by a log-normal distribution. This size distribution could indicate either a purely probabilistic size distribution process or a statistical clustering of unresolved smaller particles. Clusters are formed during and after the powder production as the silicon particles tend to agglomerate. Furthermore, compression of powders into pellets during the sample preparation also leads to further clustering of particles.

The mean particle diameter calculated using equation (6.2) and plotted in figure (6.6) shows a decrease in the average particle size with time. This is due to the continuous attrition of the particles. Also, as seen in the SEM images, a high curvature of the particles surface is achieved as a result of the high attrition rate which leads to the shape of the particles becoming more spherical with longer milling time.

EDX analysis shows that the dominant element in the high energy milled silicon nanopowder is silicon, as expected, shown by its $K\alpha$ x-ray emission at 1.739 KeV. Trace amounts of oxygen, seen by the $K\alpha$ peak at 0.525 KeV, carbon at $K\alpha = 0.282$ KeV, aluminium at $K\alpha = 1.49$ KeV, iron at $L\alpha = 0.67$ KeV, and calcium at $K\alpha = 3.59$ KeV, in the powder is also indicated. The aluminium, iron and calcium are not introduced in the milling as they were specified as impurites by the manufacturer. In the EDX spectra, most of the carbon and oxygen signals are probably due to presence of adsorbed atmospheric gases - water vapour, carbon dioxide, oxygen and light hydrocarbons. However, a small concentration of oxygen is chemically bonded to the silicon as discussed below.

EDX and XPS studies both show that the low energy ball milled silicon and the high energy milled silicon mainly contain the same types of impurities. However, figure (6.12) and (A.16)

both indicate a well defined iron photoemission peak from the steel ball milled sample, which can be attributed to contamination from the milling media.

Table (6.2) gives the oxygen concentration in the high energy milled silicon nanoparticles, and indicates that the oxygen contamination is fairly independent of milling time for a particular milling process. For the ball milled nanoparticles, there is a considerably higher oxygen level, as shown in figures (6.9) and (A.16) than for the high energy milled particles. This is most likely due to the adsorption of atmospheric gases leading to the gradual oxidation of the silicon during the milling process.

Nanoscale powders are generally believed to be heavily deformed by high energy ball milling with a large amount of strain [124] leading to the surface of the nanoparticles being unstable. However, for silicon no oxidation takes place with the size reduction during high energy milling. This can be attributed to the reduction of silicon sub-oxides by the milling media [125]. After milling, the termination of dangling bonds by oxygen stabilizes the surface of the nanoparticles against further oxidation leading to the formation of stable nanoparticles allowing charge transport through the surface.

XPS spectra for the low energy ball milled nanoparticles (figures (6.14) and (6.15)) show a strong signal from fully oxidised silicon. In figure (6.16), the Si^{4+} component for the high energy milled particles, with the bonding configuration illustrated in figure (7.4), is considerably reduced compared to the Si^{0} component. For comparison, the other oxidation states are shown in figures (7.1) to (7.3).

In general, the oxygen calculated coverage is lower for XPS than that estimated by EDX. This is probably due to the difference in the measurement techniques as EDX samples have a much thicker region, including interstices between particles, and does not differentiate adsorbed gases containing oxygen.

Zirconia ball milled silicon exhibits a relatively strong Si^{2+} component in its photoemission spectra, which corresponds to the bonding configuration illustrated in figure (7.1). In contrast, the XPS spectrum of steel ball milled silicon has a more dominant Si^{1+} component, corresponding to the bonding configuration shown in figure (7.2). The high energy milled silicon samples have

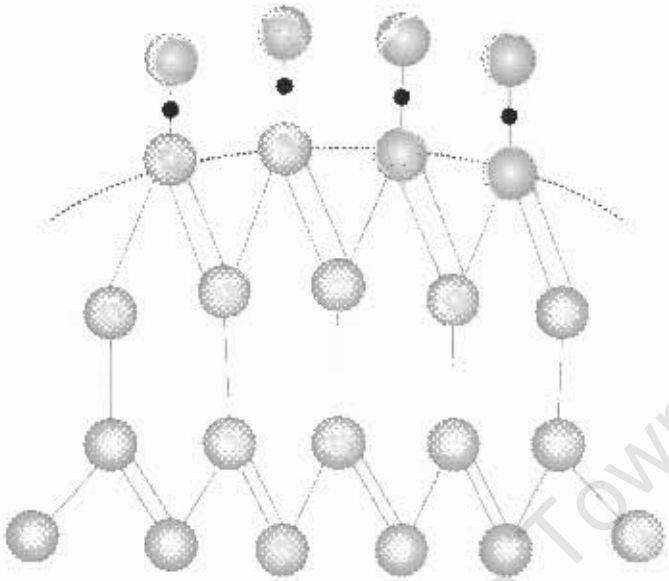

Figure 7.1 Bonding configuration of silicon atom with one oxygen neighbour [118].

components corresponding to both Si^{1+} and Si^{2+}, but very little Si^{4+} in comparison.

For the high energy milled silicon, there is no systematic variation in the intensity of the photoemission peaks of the oxidation states with respect to milling time as shown in figure (6.17). The figure also demonstrates that the fully oxidised state remains fairly constant with respect to milling time.

The results are excellent because they show that there is no formation of oxygen on the high energy milled silicon nanoparticle thereby allowing charge transport through the surface making them ideal for producing semiconducting nanocomposites particularly for printed electronics [15].

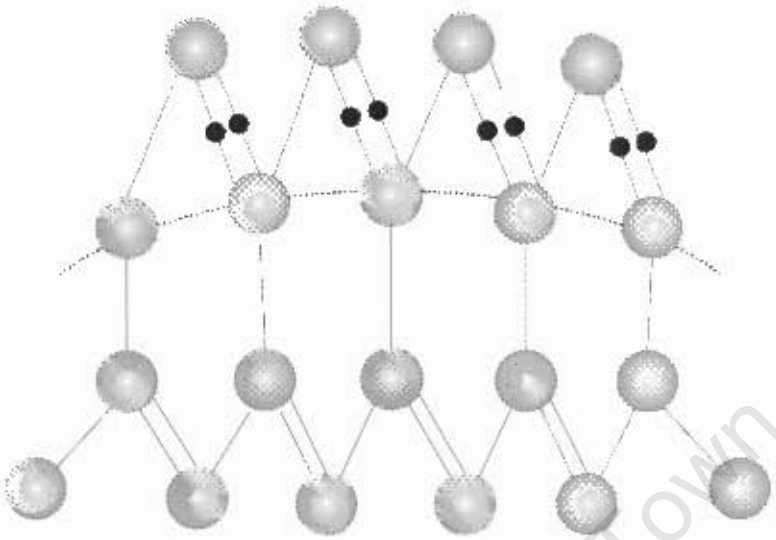

Figure 7.2: Bonding configuration of silicon atom with two oxygen neighbours [118].

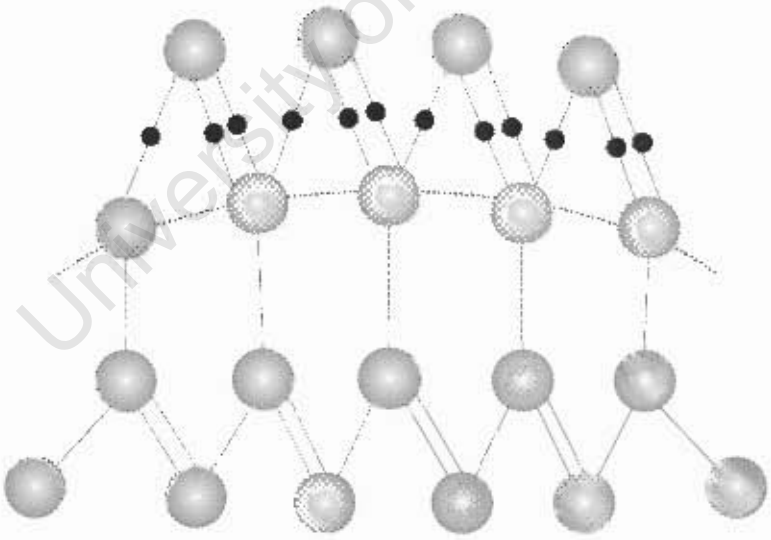

Figure 7.3: Bonding configuration of silicon atom with three oxygen neighbours [118].

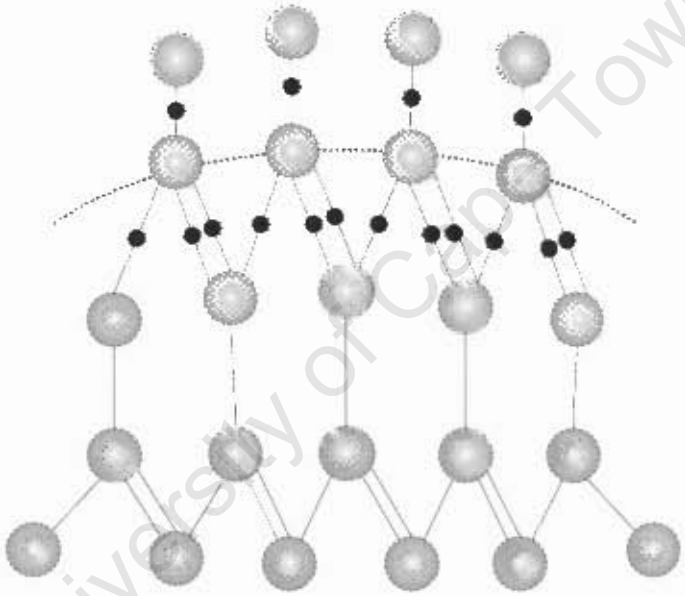

Figure 7.4: Bonding configuration of silicon atom with four oxygen neighbours [118].

8. Conclusion

The research presented in this thesis is ongoing and is aimed at studying the nature of the silicon nanoparticles produced by milling of bulk silicon. A first approach has been carried out in investigating the morphology of the nanoparticles by using scanning electron microscopy (SEM). The oxide formed on the silicon nanoparticles has also been studied using energy dispersive x-ray spectroscopy (EDX), and x-ray photoemission spectroscopy (XPS).

The morphological studies carried out using scanning electron microscopy reveal that the high energy milled silicon nanoparticles have a wide range of shapes and sizes. The shape of the particles tends to become more spherical with milling time as a result of the high attrition rate leading to a high curvature of the particle surface. The SEM micrographs and the particle size distribution show that the nanoparticles have a wide range of particle sizes, but there are a few large particles. The average particle size shows a decrease with milling time, ranging from 195 nm, for 30 minutes milling, to 119 nm after 5 hours.

Compositional studies using energy dispersive X-ray spectroscopy (EDX) and X-ray photoemission spectroscopy (XPS) reveal that the impurities present in the milled silicon nanoparticles are oxygen and carbon, in addition to trace elements initially present. The oxygen and carbon are primarily from adsorbed atmospheric gases introduced during the milling process, which was performed in air. However, ball milling with steel media introduces iron contamination in the milled nanoparticles. For all the ball milled nanoparticles there is a considerable amount of oxygen due to the gradual oxidation of the silicon during the milling process, as seen by the strong Si^{4+} photoemission peak. In contrast, the oxygen concentration in the high energy milled silicon nanoparticles is low showing that contamination during the milling process is low and that oxidation is inhibited. Stable silicon nanoparticles are produced as a result of the reduction of silicon sub-oxides by the milling media. The termination of the dangling bonds by oxygen against oxidation leads to the formation of stable nanoparticles which are not insulating, but allow charge transport through the surface.

References

[1] Lang Tran. http://www.iom-world.org/research/nanoparticles.php, Nanoparticles. Retrieved on "2008–05–06".

[2] Y. Ju-Nam and J. Lead. Manufactured nanoparticles: An overview of their chemistry, interactions and potential environmental implications. *Science of the total environment*, 2008, **400**, 396–414.

[3] E. Trave, V. Bello, F. Enrichi, G. Mattei, E. Borsella, M. Carpanese, M. Falconieri, C. Abate, N. Herlin-Boimee, K. Jursiokov, F. Costa, L. Costa, and L. Gini. Towards controllable optical properties of silicon based nanoparticles for applications in opto-electronics. *Optical Materials*, 2005, **27**, 1014–1019.

[4] K. Nishio, M. Ikeda, N. Gokon, S. Tsubouchi, H. Narimatsu, Y. Mochizuki, S. Sakamoto, A. Sandhu, M. Abe, and H. Handa. Preparation of size-controlled (30100 nm) magnetite nanoparticles for biomedical applications. *Journal of Magnetism and Magnetic Materials*, 2007, **310**, 2408–2410.

[5] W. Liu. Nanoparticles and their biological and environmental applications. *Journal of Bioscience and Bioengineering*, 2006, **103**, 1–7.

[6] A. Mastalir, Z. Kiraly, A. Patzko, I Dekany, and P. LArgentiere. Synthesis and catalytic application of Pd nanoparticles in graphite oxide. *Carbon*, 2008, **46**, 1631–1637.

[7] C. Yu, W. Oduro, K. Tam, and E. Tsang. Metallic nanoparticles. *Handbook of Metal Physics*, 2008, **5**, 1–385.

[8] C. Korsvik, S. Patil, S. Seal, and W.T. Self. Superoxide dismutase mimetic properties exhibited by vacancy engineered ceria nanoparticles. *Journal of Chemical Communication*, 2007, **10**, 1056-1058.

[9] S. Cuenot, C. Fretigny, S. Demoustier-Champagne, and B. Nysten. Surface tension effect on the mechanical properties of nanomaterials measured by atomic force microscopy. *Physical Review B*, 2004, **69**, 165410.

[10] V. Kapaklis. Structural characterization of silicon nanocrystals from amorphous silicon oxide materials. *Journal of Non-Crystalline Solids*, 2007, **354**, 612–617.

[11] K.M.M.A. El-Nour, A. Eftaiha, A. Al-Warthan, and R.A.A. Ammar. Synthesis and applications of silver nanoparticles. *Arabian journal of chemistry*, 2008.

[12] M.R. Scriba, D.T. Britton, C. Arendse, M.J. Van staden, and M. Harting. Composition and crystallinity of silicon nanoparticles synthesised by hot wire thermal catalytic pyrolysis at different pressures. *Journal of thin Solid Films*, 2009, **517**, 3484–3487.

[13] A. Reindl, A. Voronov, P.K. Gorle, M. Rauscher, A. Roosen, and W. Peukert. Dispersing and stabilizing silicon nanoparticles in a low-epsilon medium. *Colloids and Surfaces A*, 2008, **320**, 183–188.

[14] A.A. Tseng, J. Park, G.P. Vakanas, H. Wu, M. Raudensky, and T.P. Chen. Influences of interface oxidation on transmission laser bonding of wafers for microsystem packaging. *Microsystem Technologies*, 2006, **13**, 49–59.

[15] M. Härting, J. Zhang, D.R. Gamota, and D.T. Britton. Fully printed silicon field effect transistors. *Applied Physics letters*, 2009, **94**, 193509.

[16] M.L. Ostraat, M. Brongersma, H.A. Atwater, and R.C. Flagan. Nanoengineered silicon/silicon dioxide nanoparticle heterostructures. *Solid State Sciences*, 2005, **7**, 882–890.

[17] A. Ainyette. *Synthesis of semiconductor nanoparticles*. Neuroscience, Washington, 2006.

[18] G. Yordanov, D. Dushkin, D. Gicheva, H. Bochev, and E. Adachi. Synthesis of high-quality semiconductor nanoparticles in a composite hot-matrix. *Chemistry and Materials Science*, 2005, **284**, 229–232.

[19] N.L. Pickett and P. OBrien. Synthesis of semiconductor nanoparticles using single-molecular precursors. *Chemical Record*, 2001, **1**, 467–479.

[20] M.P. Neupane, Y.K. Kim, S. Park, K.A. Kim, M.A. Lee, and T.S. Bae. Temperature driven morphological changes of hydrothermally prepared copper oxide nanoparticles. *Journal of Surface and Interface Analysis*, 2009, **41**, 259–263.

[21] J. Perriere, E. Million, and E. Fogarassy. *Recent advances in laser processsing of materials.* Elsevier, Amsterdam, 2006.

[22] H. Warad, A. Suhane, Y. Boontongkong, C. Thanachayanont, and J. Dutta. Colloidal Synthesis of Semiconductor Nanoparticles. *Proceedings of the Third Thailand Materials Science and Technology Conference (MSAT III)*, 2004, 16–18.

[23] SciTech Dictionary. http://www.answers.com/topic/quantum-dot, Quantum confinement in solids. Retrieved on "2011–05–04".

[24] R. Kelsall, I. Hamley, and M. Geoghegan. *Nanoscale Science and Technology.* John Wiley, NJ, 2005.

[25] K.J. Koski, N.M. Kamp, R.K. Smith, M. Kunz, J.K. Knight, and A.P. Alivisatos. Structural distortions in 510 nm silver nanoparticles under high pressure. *Physical Review B*, 2008, **78**, 165410.

[26] H. Ikemoto, A. Goyo, and T. Miyanaga. Size dependence of the local structure and atomic correlations in tellurium nanoparticles. *Physical Chemistry*, 2011, **115**, 2931–2937.

[27] C.S. Palenik, S. Utsunomiya, M. Reich, S.E. Kesler, L. Wang, and R. Ewing. Invisible gold revealed. Direct imaging of gold nanoparticles in a Carlin-type deposit. *American Mineralogist*, 2004, **89**, 1359–1366.

[28] R. Goswami and K. Chattopadhyay. Melting of Bi nanoparticles embedded in a Zn matrix. *Acta Materialia*, 2004, **52**, 5503–5510.

[29] C. Binns. *Introduction to Nanoscience and Nanotechnology.* John Wiley, NJ, 2010.

[30] S.V.N.T. Kuchibhatla, A.S. Karakoti, and S. Seal. One dimensional nanostructured materials. *Progress in Material Science*, 2006, **52**, 699–913.

[31] N.S. Mani. *Applied Physics.* Pearson Education, India, 2010.

[32] Z.H. Khan. Electrical and optical properties of thin film of amorphous silicon nanoparticles. *Applied Surface Science*, 2009, **255**, 8874–8878.

[33] J. Kocka, I. Pelant, and A. Fejfar. Light emitting silicon, recent progress. *Journal of Non-Crystalline Solids*, 1996, **198**, 857–862.

[34] J. de Wild, A. Meijerink, J.K. Rath, W. Van Sark, and R. Schropp. Towards upconversion for amorphous silicon solar cells. *Solar Energy Materials and Solar Cells*, 2010.

[35] X. Huang and Y. Choi. Chemical sensors based on nanostructured materials. *Sensors and Actuators B*, 2007, **122**, 659–671.

[36] M.R. Scriba, C. Arendse, M. Härting, and D.T. Britton. Hot-wire synthesis of Si nanoparticles. *Thin Solid Films*, 2008, **516**, 844–846.

[37] G. Spencer, B. Anyamesem-Mensah, H.C. Galloway, A. Bandyopadhyay, and D. Frasier. Silicon nanoparticle synthesis by short-period thermal anneals at atmospheric pressure in argon. *Journal of Vacuum Science and Technology A*, 2011, **29**, 051508.

[38] I. Sandu, P. Moreau, D. Guyomard, T. Brousse, and L. Roue. Synthesis of nanosized Si particles via a mechanochemical solid-liquid reaction and application in Li-ion batteries. *Journal of Solid State Ionics*, 2007, **178**, 1279–1303.

[39] C. Lam, Y.H. Zhang, C.S. Lee, I. Bello, and S.T Lee. Large scale synthesis of untrafine si nanoparticles by ball milling. *Journal of crystal growth*, 2000, **220**, 466–470.

[40] A. Marikani. *Engineering Physics*. Raj, New Delhi, 2009.

[41] A. Odo. *Synthesis, Characterisation and Device Application of Silicon Nanoparticles produced by Mechanical Attrition*. PhD thesis, University of Cape Town, 2009.

[42] Z. Zhong, B. Gates, and Y. Xia. Soft Lithographic Approach to the Fabrication of Highly Ordered 2D Arrays of Magnetic Nanoparticles on the Surfaces of Silicon Substrates. *American Chemical Society*, 2000, **16**, 10369–10375.

[43] A.M. Contrera, J. Grunes, X. Yan, A. Liddle, and G.A. Somorjai. Fabrication of platinum nanoparticles and nanowires by electron beam lithography (EBL) and nanoimprint lithography (NIL): comparison of ethylene hydrogenation kinetics. *Catalysis Letters*, 2005, **100**, 3–4.

[44] J.C. Ion. *Laser processing of engineering materials.* Elsevier, Oxford, 2006.

[45] J.E. Munoz, J. Cervantes, R. Esparza, and G. Rosas. Iron nanoparticles produced by high-energy ball milling. *Journal of Nanoparticle Research*, 2007, **9**, 945–950.

[46] C.L. De Castro and B.S. Mitchell. Nanoparticles from Mechanical Attrition. *American Scientific Publishers*, 2002.

[47] C.C. Koch. Structural nanocrystalline materials: an overview. Journal of material science. *Journal of Material Science*, 2006, **42**, 1403–1414.

[48] H.A. Pearson. *Handbook of chemical vapor deposition (CVD): Principles, technology and applications.* Noyes, New York, 1992.

[49] H. Grimm, N. Petermann, A. Gupta, and H. Wiggers. *Synthesis of highly doped silicon and germanium nanoparticles in a low-pressure plasma-reactor for thermoelectric and plasma reactors.* University of Duisburg-Essen, DE.

[50] C.E. Morosanu. *Thin Films by Chemical Vapour Deposition.* Elsevier, Bucharest, 1990.

[51] L.L. Shaw. Processing nanostructured materials: an overview. *Journal of Minerals, Metals, and Materials Society*, 2000, **9**, 41–45.

[52] Y. Kamlag, A. Goossens, I. Coolbeck, and J. Schoonman. Laser cvd of cubic sic nanocrystals. *Journal of Applied Surface Science*, 2001, **184**, 118–122.

[53] O. Alm, L. Landstrom, M. Boman, C. Granqvist, and P. Heszler. Tungsten oxide nanoparticles synthesised by laser assisted homogeneous gas-phase nucleation. *Journal of Applied Surface Science*, 2005, **247**, 1–4.

[54] Michael Anissimov. http://www.wisegeek.com, Chemical vapour deposition. Retrieved on "2009–11–16".

[55] G.V. Karas. *New developments in crystal growth research.* Nova Science, New York, 2005.

[56] J.A. Rodrguez and M.F. Garca. *Synthesis, properties, and applications of oxide nanomaterials.* John Wiley, NJ, 2007.

[57] K.M. Lee, D.J. Lee, and H. Ahn. XRD and TEM studies on tin oxide (II) nanoparticles prepared by inert gas condensation. *Materials Letters*, 2004, **58**, 3122–3125.

[58] R. Mueller, L. Madler, and S.E. Pratsinis. Nanoparticle synthesis at high production rates by flame spray pyrolysis. *Chemical Engineering Science*, 2003, **58**, 1969–1976.

[59] G. Skandan, Y.J. Chen, and B.H. Kear. Synthesis of oxide nanoparticles in low pressure flames. *Nanostructured Materials*, 1999, **11**, 149–158.

[60] S.L Girshick. Aerosol processing for nanomanufacturing. *Journal of*, 2008, **10**, 935–945.

[61] J. Manners. *An introduction to Quantum Physics*. IOP, Bristol, 2000.

[62] S. Sharma. *Atomic and Nuclear Physics*. Dorling Kindersley, India, 2008.

[63] P. Echlin. *Low-temperature Microscopy and Analysis*. 1992. Plenum, New York.

[64] D. Stokes. *Principles and practice of variable pressure/environmental scanning electron microscopy (VP-ESEM)*. John Wiley, UK, 2008.

[65] S. Buys and V. Oakley. *Conservation and Restoration of Ceramics*. 1996. Butterworth-Heinemann, London.

[66] sck. http://www.sckcen.be/microstructure/infrastructure/sem, Backscattered electrons. Retrieved on "2009–11–16".

[67] Jie He. http://www.scribd.com, Scanning electron microscopy. Retrieved on "2009–11–16".

[68] EMAL. http://www.emal.engin.umich.edu, SEM lectures. Retrieved on "20–05–2008".

[69] M.F. L'Annunziata, M.M. Elbaradei, and W. Burkart. *Handbook of Radioactivity Analysis*. 2003. Academic, California.

[70] R.A. Serway, J.S. Faughn, and C. Vuille. *College Physics*. Cengage learning, Canada, 2009.

[71] C.M. Langton. *The Physical Measurement of Bone*. 2004. IOP, London.

[72] UCDAVIS. http://safetyservices.ucdavis.edu, Physics of X-ray Production. Accessed on "20–05–2008".

[73] C. Suryanayrayana and N.G. Norton. *X-ray Diffraction: A Practical Approach*. Plenum Press, New York, 1998.

[74] C.P. Poole and C.P. Poole Jr. *The Physics Handbook: Fundamentals and Key Equations*. 1998. Wiley, Weinheim.

[75] wikipedia. http://en.wikipedia.org/wiki/bremsstrahlung, Bremsstahlung. Accessed on "20–05–2008".

[76] M. Schultz. *Multiple View 3D Reconstruction of Micro to Nano Scopic Specimens*. University of Tennessee, 2004.

[77] Scanning electron microscope. http://scanning-electron-microscope.co.tv/cathodoluminescence, Cathodoluminescence. Retrieved on "2011–05–04".

[78] C. Leroy and P.G. Rancoita. *Principles of radiation interaction in matter and detection*. World scientific publishing, London, 2004.

[79] K. Janssens and R. Grieken. *Non-destructive microanalysis of cultural heritage materials*. Elsevier, Amsterdam, 2004.

[80] P. Dendy and B. Heaton. *Physics for diagnostic radiology*. IOP, Bristol, 1999.

[81] F. Campeau and J. Fleitz. *Limited Radiography*. Cencage, New York, 2009.

[82] G.F. Knoll. *Radiation Detection and Measurement*. John Wiley and Sons. Inc., New Jersey, 2010.

[83] HUJ. http://www.einsteinyear.org/facts/photoelectriceffect/, Photoelectric Effect. Accessed on "20–05–2008".

[84] Dual nature of radiation and matter. http://www.tutorvista.com/content/physics/physics-iv/radiation-and-matter/photoelectric-effect-and-cell.php, Photoelectric effect and cell animation. Retrieved on "2011–05–04".

[85] N.H. Malik. *Engineering Physics*. Tata Mcgraw Hill, New Delhi, 2009.

[86] John Smith. http://anshsphysics.wordpress.com, Photoelectric effect. Retrieved on "2009–11–16".

[87] NDT. http://www.ndt-ed.org/educationresources/communitycollege/radiography/physics/comptonsc Compton Scattering. Accessed on "20–05–2008".

[88] M.V. Heimendahl. *Electron microscopy of materials*. Academic Press, NY, 1980.

[89] E.M. Slayter and H.S. Slayter. *Light and Electron Microscopy*. Cambridge University Press, Cambridge, 1998.

[90] T.G. Rochow and E.G. Rochow. *An Introduction to Microscopy by means of Light, Electrons, X-rays, or Ultrasound*. Plenum, New York, 1978.

[91] R.J. Oldfield and R. Oldfield. *Light Microscopy: An Illustrated Guide*. 1994. Wolfe Publishing, London.

[92] P.J. Grundy and G.A. Jones. *Electron microscopy in the study of materials*. Edward Arnold, London, 1976.

[93] C. Jerry. *The World Under the Microscope*. 1974. Orbis Books, London.

[94] Ilya Sherman. http://www.hypertextbook.com, Resolution of an electron microscope. Accessed on "20–09–2009".

[95] L.M. Brown, A. Pais, and A.B. Pippard. *Twentieth Century Physics*. 1995. IOP, London.

[96] S. Amelinckx, D. Van Dyck, J. Van Landuyt, and G. Van Tendeloo. *Electron Microscopy Principles and Fundamentals*. Wiley, Weinheim, 1997.

[97] M. Wilson, K. Kannangara, G. Smith, M. Simmons, and B. Raguse. *Nanotechnology : Basic science and emerging technologies*. CRC Press, FL, 2002.

[98] H. Butt, K. Graf, and M. Kappl. *Chemistry of interfaces*. John Wiley, Weinheim, 2003.

[99] P.J. Goodhew, F.J. Humphreys, and R. Beanland. *Electron microscopy and analysis*. Taylor and Francis, London, 2001.

[100] S. Christian. *Correlation between raman spectroscopy and electron spectroscopy on individual carbon nanotubes and peapods*. Julich, Duisberg, 2010.

[101] Babcock and Wilcox. http://www.babcock.com/services/laboratory-management-and-services/semlab.html, Laboratory Management and Services: Scanning Electron Microscopy Laboratory. Accessed on "20–05–2008".

[102] J.M. Jaklevic and F.S. Goulding. *Energy Dispersion, in X-ray Spectrometry (Herglotz, H.K. and Birks, L.S. and Eds.)*. Marcel Dekker, Inc., New York, 1978.

[103] MEE. http://mee-inc.com/eds.html, Energy dispersive x-ray spectroscopy. Accessed on "20–09–2009".

[104] Christopher Walker. http://www.uksaf.org/tech/edx.html, Energy Dispersive X-ray. Retrieved on "2009–11–16".

[105] V.I. Nefedov. *X-ray Photoelectron Spectroscopy of Solid Surfaces*. Alden Press, Oxford, 1988.

[106] W. Andreoni. *The physics of fullerene based and fullerene related materials*. Kluwer Academic, Boston, 2000.

[107] L. Brillson. *Surfaces and Interfaces of Electronic Materials*. Wiley, Weinheim, 2010.

[108] wiki. http://en.wikipedia.org/wiki/photoemission-spectroscopy, Photoemission spectroscopy. Retrieved on "2011–01–12".

[109] A.N. Goldstein. *Handbook of Nanophase Materials*. Marcel Dekker Inc., New York, 1997.

[110] J.C. Riviere and M.P. Seah. http://www.kayelaby.npl.co.uk, X-ray Photoemission spectroscopy. Retrieved on "03–12–2009".

[111] ASM. *Characterisation and Failure Analysis of Plastics*. ASM International, USA, 2003.

[112] S. Rao. *Surface Chemistry of Froth Flotation*. Kluwer Academic, New York, 2004.

[113] J.P. Bonnelle, B. Delmon, and E.G. Derouane. *Surface properties and catalysis by non-metals*. Reidel, Dordrecht, 1983.

[114] D. Shi. *Biomaterials and Tissue Engineering*. Springer, NY, 2004.

[115] D.T. Britton and M. Harting. Printed nanoparticulate composites for silicon thick-film electronics. *Pure Applied Chemistry*, 2006, **78**, 1723–1739.

[116] A.L. Johnson, G.D. Ackerman, M.R. Howells, Z. Hussain, H.A. Padmore, T.R. Renner, W. Steele, F. Gozzo, B. Triplett, R. Ynzunza, P.D. Kinney, R. Odom, and E. Principe. Comparison between the μXPS Endstation and the PHI Quantum 2000. *Advanced light source user abstract, 1997, http://www.als.lbl.gov/compendium/abstractManager/uploads/comparison.pdf*, Accessed on 06/10/2011.

[117] M. Niwano, H. Katakura, Y. Takeda, Y. Takakuwa, N Miyamoto, A. Hiraiwa, and K. Yagi. Photoemission study of the SiO_2/Si interface structure of thin oxide films on Si(100), (111), and (110) surfaces. *Journal of Vacuum Science and Technology A9*, 1991, 195–200.

[118] K. Hirose, H. Nohira, K. Azuma, and T. Hattori. Photoelectron spectroscopy study of SiO_2/Si interfaces. *Progress in Surface Science*, 2007, **82**, 3–54.

[119] ImageJ. http://rsb.info.nih.gov/ij/, Image Processing Software. Retrieved on "2010–1–05".

[120] R. Billinton and R. Allan. *Reliability evaluation of engineering systems: Concepts and techniques*. Plenum Press, New York, 1992.

[121] C.C. Koch. Top-down synthesis of nanostructured materials: Mechanical and thermal processing methods. *Reviews on Advanced Materials Science*, 2003, **5**, 91–92.

[122] B.Q. Han, E.J. Lavernia, and F.A. Mohammed. Mechanical properties of nanostructured materials. *Reviews on Advanced Materials Science*, 2005, **9**, 1–16.

[123] Kevex International Corp. *Analytical Instrument Division*. Perrygraf Corp., 1974.

[124] S.S. Chen, C.P. Yang, Z.H. Zhou, D.H. Guo, H. Wang, and G.H. Rao. Synthesis of Nd0.7Sr0.3MnO3 ceramics by high-energy ball milling. *Journal of Alloys and Compounds*, 2008, **463**, 271-274.

[125] D.T. Britton and M. Härting. Semiconducting nanoparticles with surface modification, WO20100148144PCT(Patent Document), 2010.

[126] F.S. Diana, S.H. Lee, P.M. Petroff, and E.J. Kramer. Fabrication of hcp-Co Nanocrystals via Rapid Pyrolysis in Inverse PS-b-PVP Micelles and Thermal Annealing. *Journal of American Chemical Society*, 2003, **3**, 891-895.

[127] H.S. Uh, S.W. Ko, and J.D. Lee. Growth and field emission properties of carbon nanotubes on rapid thermal annealed Ni catalyst using PECVD. *Diamond and Related Materials*, 2005, **14**, 850–854.

[128] A.U. Limaye and J.J. Helble. Morphological control of zirconia nanoparticles through combustion aerosol synthesis. *Journal of American Ceramic Society*, 2002, **85**, 1127.

[129] Y. He, X. Li, and M.T. Swihart. Laser-driven aerosol synthesis of nickel nanoparticles. *Journal of Chemistry of Materials*, 2005, **17**, 1017–1026.

[130] B. Zhao, Z. Yang, Z. Li, M.V. Johnston, and H. Wang. Particle size distribution function of incipient soot in laminar premixed ethylene flames: effect of flame temperature. *Proceedings of the Combustion Institute*, 2005, **30**, 1441-1448.

[131] D.R. Hamann. Energetics of silicon suboxides. *Physical Review B*, 1999, **61**, 9899–9901.

[132] H. Zhou, H.K. Kim, F.G. Shi, B. Zhao, and J. Yota. Optical properties of PECVD dielectric thin films: thickness and deposition method dependence. *Journal of Microelectronics*, 2002, **33**, 999–1004.

[133] J. Appenzeller, R. Martel, P. Solomon, K. Chan, P. Avouris, J. Knoch, J. Benedict, M. Tanner, S. Thomas, K.L. Wang, and J.A. del Alamo. A 10 nm MOSFET concept. *Microelectronic Engineering*, 2001, **56**, 213–219.

[134] S. Oosterhoff and J. Middelhoek. The annealing of 1 mev implantations of boron in silicon. *Solid-State Electronics*, 1985, **28**, 427–433.

[135] B. Baretzky, M.D. Baro, G.P. Grabovetskaya, J. Gubicza, M.B. Ivanov, Yu.R. Kolobov, T.G. Langdon, J. Lendvai, A.G. Lipnitskii, A.A. Mazilkin, A.A. Nazarov, J. Nogues, I.A. Ovidko, S.G. Protasova, G.I. Raab, A. Revesz, N.V. Skiba, J. Sort, M.J. Starink, B.B. Straumal, S. Surinach, T. Ungar, and A.P. Zhilyaev. Fundamentals of interface phenomena in advanced bulk nanoscale materials. *Reviews on Advanced Materials Science*, 2005, **9**, 45–108.

[136] J. Graetz, C.C. Ahn, R. Yazami, and B. Fultz. Highly reversible lithium storage in nanostructured silicon. *Journal of solid state electrochemistry*, 2003, **6**, A194–197.

[137] T. He, M. Lu, J. He, B. Chen, N.H. Di Spigna, D.P. Nackashi, P.D. Franzon, and J.M. Tour. Reversible modulation of conductance in silicon devices via UV and visiblelight irradiation. *Advanced materials*, 2008, **20**, 1–6.

[138] Z. Kang, C.H.A. Tsang, N. Wong, Z. Zhang, and S. Lee. Silicon quantum dots: A general photocatalyst for reduction, decomposition, and selective oxidation reactions. *Journal of the american chemical society*, 2007, **129**, 12090-12091.

[139] M. Swihart. Vapor-phase synthesis of nanoparticles. *Journal of colloid and interface science*, 2003, **8**, 127–133.

[140] F. Kruis, H. Fissan, and A. Peled. Synthesis of nanoparticles in the gas phase for electronic, optical and magnetic applications. *Journal of Aerosol Science*, 1998, **329**, 511–535.

[141] R. Kakkad, J. Smith, W.S. Lau, S.J. Fonash, and R. Kerns. Crystallized Si films by low temperature rapid thermal annealing of amorphous silicon. *Journal of Applied Physics*, 1989, **65**, 2069.

[142] B.A. Joyce and T.B. Joyce. Basic studies of molecular beam epitaxy - past, present and some future directions. *Journal of Crystal Growth*, 2004, **264**, 605–619.

[143] M.A. Barakat, G. Hayes, and S. Ismat Shah. Effect of cobalt doping on the phase transformation of TiO2 nanoparticles. *Journal of Nanoscience and Nanotechnology*, 2005, **5**, 795–765.

[144] H. Warad, S.C. Ghosh, B. Hemtanon, C. Thanachayanont, and J. Dutta. Luminescent nanoparticles of Mn doped ZnS passivated with sodium hexametaphosphate. *Science and Technology of Advanced Materials*, 2005, **6**, 296-301.

[145] J.E. Fair. Rapid thermal processing for active matrix devices. 1992, **35**, 47.

[146] C.T. Foxon. Three decades of molecular beam epitaxy. *Journal of Crystal Growth*, 2003, **251**, 1–8.

[147] S.W. Cho, J.H. Yun, D.H. Jun, J.I. Song, I. Adesida, N. Pan, and J.H. Jang. High performance InP/InAlAs/GaAsSb/InP double heterojunction bipolar transistors. *Solid-State Electronics*, 2006, **50**, 902–907.

[148] C.C. Striemer, R. Krishnan, and P.M. Fauchet. The development of nanocrystalline silicon for emerging microelectronic and nanoelectronic applications. *Journal of the Minerals, Metals and Materials Society*, 2004, **50**, 20–25.

[149] M. Salerno, P. Landoni, and R. Verganti. Designing foresight studies for Nanoscience and Nanotechnology (NST) future developments. *Technological Forcasting and Social Change*, 2007, **75**, 1202–1223.

[150] N. Malanowski and A. Zweck. Bridging the gap between foresight and market research. *Technological forecasting and Social Change*, 2007, **74**, 1805–1822.

[151] J. El Boucham, F. Maury, and R. Morancho. Thermal decomposition mechanisms of tetraethylgermane in metal-organic chemical vapor deposition. *Journal of Analytical and Applied Pyrolysis*, 1998, **44**, 153–165.

[152] C.R. Kleijn, K.J. Kuijlaars, and H.E.A. Van Den Akker. Design and scale-up of chemical vapour deposition reactors for semiconductor processing. *Chemical Engineering Science*, 1996, **51**, 2119–2128.

[153] S.L. Girshick. Aerosol processing for nanomanufacturing. *Journal of Nanoparticle Research*, 2007, **10**, 935–945.

[154] J.S. Benjamin. Mechanical Alloying. *Scientific American*, 1976, **234**, 40.

[155] T. Trindade, P. O'brien, and N.L. Pickett. Synthesis of Semiconductor Nanoparticles. *Chemistry of materials*, 2001, **13**, 3843–3858.

[156] M.L. Lavcevic and Z. Ogorelec. Melting and solidification of Sn-clusters. *Material Letters*, 2003, **57**, 4134-4139.

[157] A. Cervellino, C. Giannini, and A. Guagliardi. Determination of nanoparticle structure type, size and strain distribution from x-ray data for monatomic f.c.c.-derived non-crystallographic nanoclusters. *Journal of Applied Crystallography*, 2003, **36**, 1148–1158.

[158] J. Zhao, X. Chen, and G. Wang. Critical size for a metal-nonmetal transition in transition-metal clusters. *Physical Review B*, 1994, **5**, 15424-15426.

[159] J. Zhao, X. Chen, Q. Sun, F. Liu, G. Wang, and K.D. Lain. Tight-binding study of the structural and magnetic properties of vanadium clusters. *Physica B: Condensed Matter*, 1995, **215**, 377–382.

[160] H. Morisaki, H. Hashimoto, F.W. Ping, H. Nozawa, and H. Ono. Strong blue light emission from an oxygen-containing Si fine structure. *Journal of Applied Physics*, 1993, **74**, 2977–2999.

[161] K.A. Littau, P.J. Szajowski, A.J. Muller, A.R. Kortan, and L.E. Brus. A luminescent silicon nanocrystal colloid via a high-temperature aerosol reaction. *Journal of Physical Chemistry*, 1993, **97**, 1224-1230.

[162] Y. Kanemitsu, H. Uto, Y. Masumoto, and Y. Maeda. On the origin of visible photoluminescence in nanometer-size Ge crystallites. *Applied Physics Letters*, 1992, **61**, 2187-2189.

[163] T. Shimizu-Iwayama, S. Nakao, and K. Saitoh. Visible photoluminescence in Si+ implanted thermal oxide films on crystalline Si. *Applied Physics Letters*, 1994, **65**, 1814-1816.

[164] X. Ju, J. Zhang, K.W. Wu, Y.J. Hou, P.H. Xie, and B.W. Zhang. Evidence for change of the interfacially local structure of titanium oxide /bis ruthenium nanocomposite. *Journal of Surface and Interface Analysis*, 2000, **32**, 95–97.

[165] V. Leshchynsky. Nanostructuring in powder metallurgy and forging technologies. *Proceedings of the 17th international scientific and technical conference*, 2008, 67–83.

[166] EMSL. http://www.emsl.pnl.gov/capabilities/viewinstrument.jsp?id=1023, Electron spectrometer: scanning xps microprobe, high resolution (quantera). Retrieved on "2011–01–12".

[167] wikipedia. http://en.wikipedia.org/wiki/scanning-electron-microscope, Scanning electron microscope. Retrieved on "2009–11–16".

[168] C. Soles. http://www.nist.gov/msel/polymers, Nanoimprint. Retrieved on "2010–05–19".

[169] Cambridge Encyclopedia. http://encyclopedia.stateuniversity.com, Photoemission Spectroscopy. Retrieved on "03–12–2009".

[170] GATAN. http://www.gatan.com/, SEM Products. Retrieved on "2008–05–06".

[171] M. Abramowitz. http://www.micro.magnet.fsu.edu, Introduction to Microscopy. Retrieved on "2008–05–06".

[172] B.C. Breton. http://www2.eng.cam.ac.uk/ bcb/history.htm, The Early History and Development of the Scanning Electron Microscope. Retrieved on "2008–05–06".

[173] ISU. http://www.mse.iastate.edu/microscopy/source.html, The Electron Source. Accessed on "20–05–2008".

[174] R.J. Budnitz and M.S. Quinby-Hunt. *Instrumentation for environmental monitoring: Water*. John Wiley, California, 1986.

[175] J. Bottero. *Environmental nanotechnology. Applications and impacts of nanomaterials*. Springer, NY, 2004.

[176] M. Roco and W. Brainbridge. *Societal implications of nanoscience and nanotechnology*. Kluwer Academic, Boston, 2001.

[177] C. Holbrow, J. Lloyd, and J. Amato. *Modern Introductory Physics*. Springer, New York, 1999.

[178] J. Bishop. *How to Win the Nobel Prize: An Unexpected Life in Science*. Harvard University Press, London, 2003.

[179] C. Warren and W. Chan. *Bio-applications of nanoparticles*. Springer Science, Texas, 2007.

[180] B. Sivasankar. *Engineering Chemistry*. Tata-McGraw Hill, New Delhi, 2008.

[181] B.D. Stojanovic, V.V. Skorokhod, and M.V. Nikolic. *Advanced science and technology of sintering*. Kluwer Academic, New York, 1999.

[182] R.W. Kelsall, I. Hamley, and M. Geoghegan. *Nanoscale Science and Technology*. John Wiley, NJ, 2005.

[183] B. Bhushan. *Springer handbook of nanotechnology*. Springer, New York, 2007.

[184] R.F.C. Farrow. *Molecular beam epitaxy: applications to key materials*. Noyes, NJ, 1995.

[185] N. Serpone, D. Lawless, and Pelizzetti E. *Fine Particles Science and Technology from Micro to Nanoparticles*. Kluwer Academic, Dordrecht, 1996, 657.

[186] R.F. Egerton. *Physical principles of electron microscopy-An introduction to TEM, SEM, and AEM*. Springer, New York, 2005.

[187] L.R. Radovic. *Chemistry and Physics of Carbon*. CRC Press, FL, 2004.

[188] P.A. Charles and FD Seward. *Exploring the X-ray Universe*. Cambridge University Press, Cambridge, 1995.

[189] R. Jenkins, R.W. Gould, and D. Gedcke. *Quantitative X-ray Spectrometry*. Marcel Dekker Inc., New York, 1995.

[190] L. Solymer and D. Walsh. *Electrical Properties of Materials*. Oxford University Press, Oxford, 1998.

[191] R.K. Bock and A. Vasilescu. *The particle detector briefbook*. 1998. Springer, New York.

[192] M. Schmidt and S.S. Sheiko. *New Developments in Polymer Analytics II*. 2000. Springer, New York.

[193] L.S. Lerner. *Modern Physics for Scientists and Engineers: : [Relativity]*. 1996. Jones and Bartlett Publishers, London.

[194] K.W. Busch and M.A. Busch. *Multielement Detection Systems for Spectrochemical Analysis*. 1990. Wiley, New York.

[195] J. Goldstein, D.E. Newbury, D.C. Joy, and C.E. Lyman. *Scanning Electron Microscopy and X-ray Microanalysis*. 2003. Plenum, New York.

Appendix A. Appendices

A.1 SEM Results

A.1.1 Micrographs of high energy milled silicon.

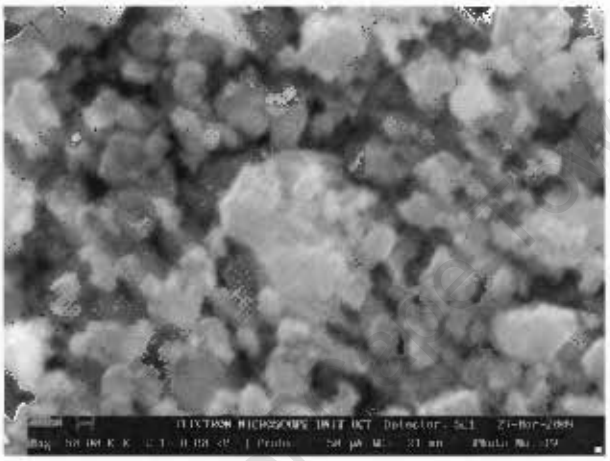

Figure A.1: A micrograph of the 2503 grade silicon milled for 1 hr.

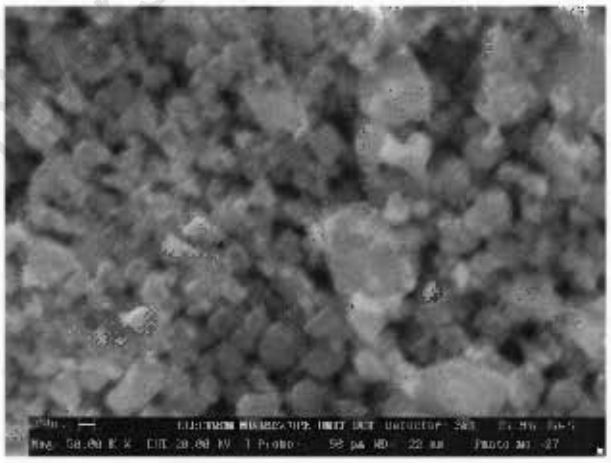

Figure A.2: A micrograph of the 2503 grade silicon milled for 2 hrs.

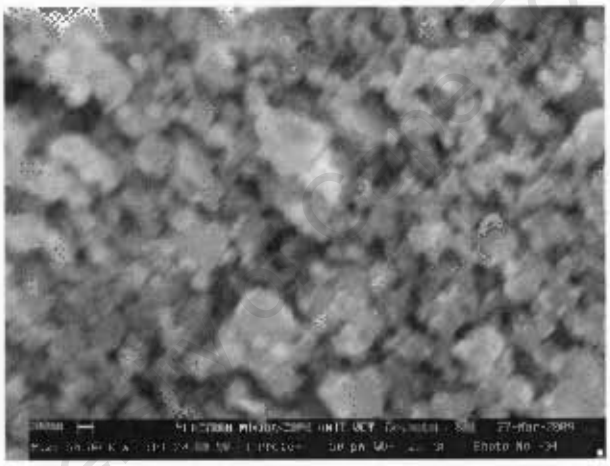

Figure A.3: A micrograph of the 2503 grade silicon milled for 3 hrs.

A.1.2 Profiles from line scans across micrographs of high energy milled silicon.

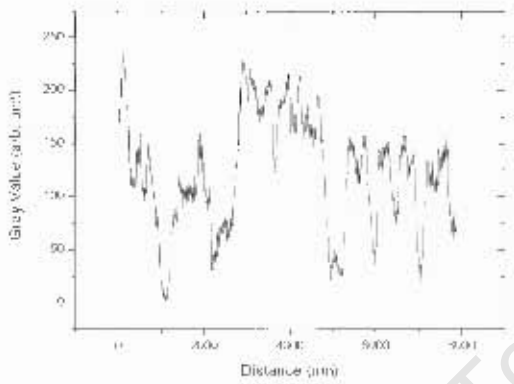

Figure A.4: Profile from a line scan across the micrograph of 2503 grade silicon milled for 1 hr.

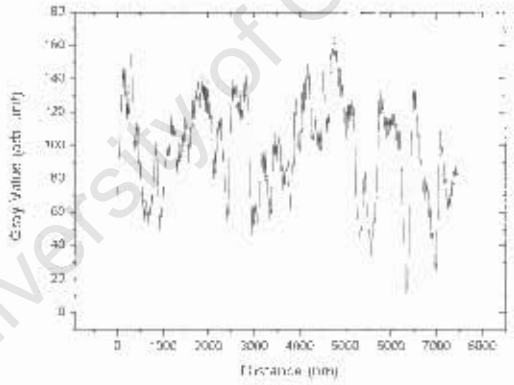

Figure A.5: Profile from a line scan across the micrograph of 2503 grade silicon milled for 2 hrs

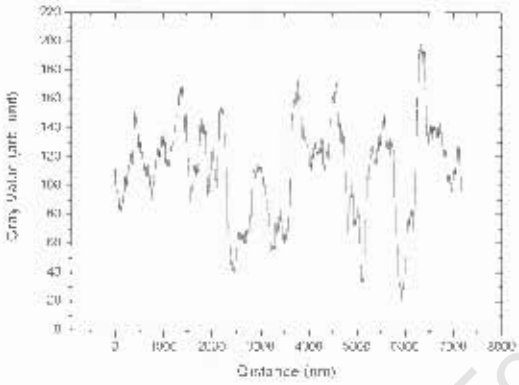

Figure A.6: Profile from a line scan across the micrograph of 2503 grade silicon milled for 3 hrs.

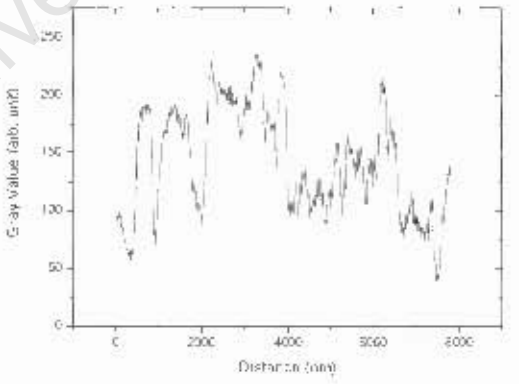

Figure A.7: Profile from a line scan across the micrograph of 2503 grade silicon milled for 5 hrs.

A.1.3 Particle size distributions of high energy milled silicon.

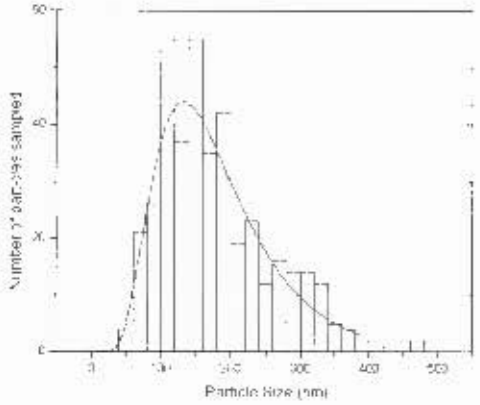

Figure A.8: Particle size distribution of the silicon milled for 1 hr.

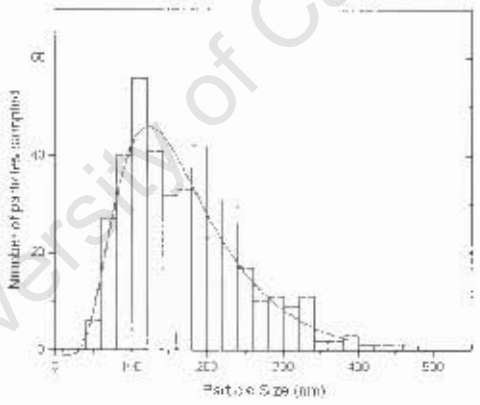

Figure A.9: Particle size distribution of the silicon milled for 2 hrs.

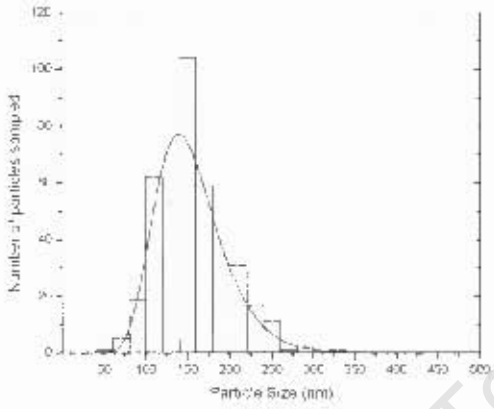

Figure A.10: Particle size distribution of the silicon milled for 3 hrs.

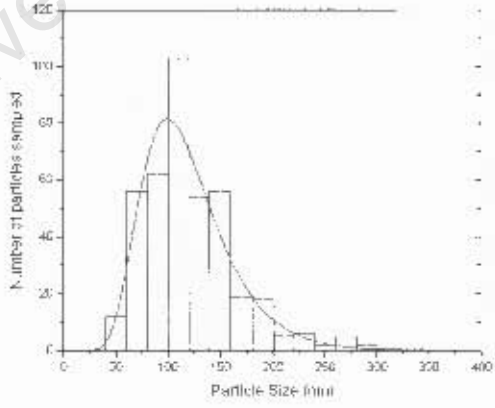

Figure A.11: Particle size distribution of the silicon milled for 5 hrs.

A.2 EDX and XPS Results

A.2.1 EDX plots for high energy milled silicon.

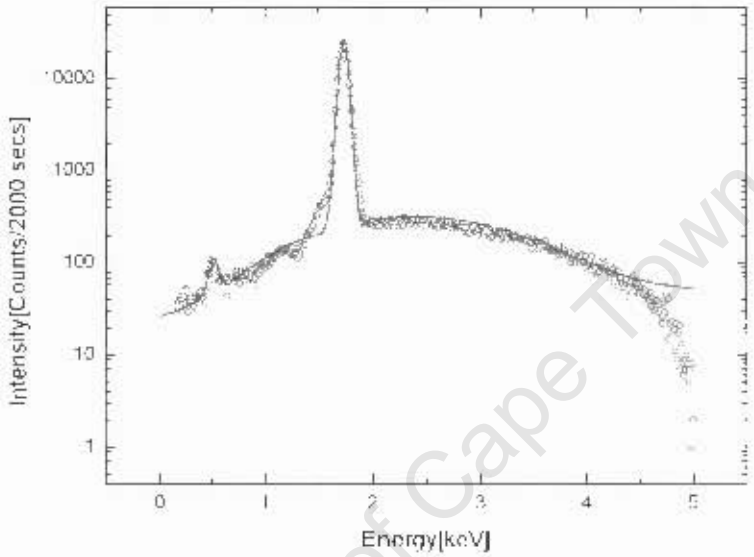

Figure A.12: Energy dispersive X-ray spectra of 2503 grade silicon milled for 30 mins. The solid line is a least squares fit to the data.

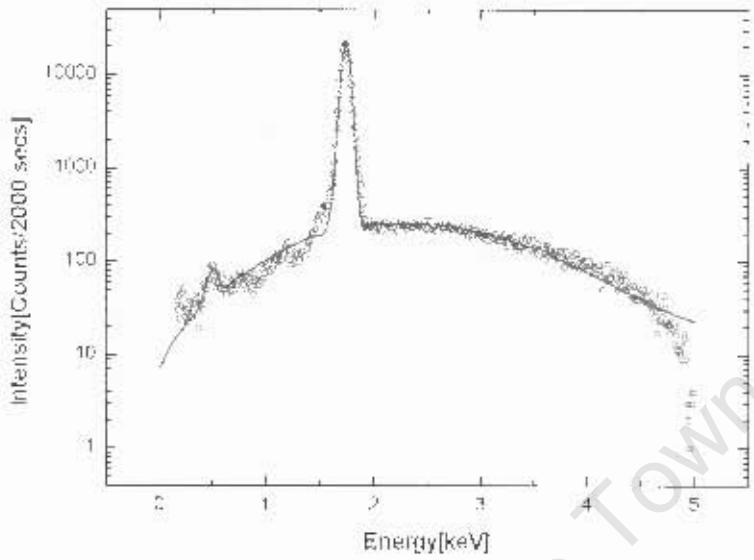

Figure A.13: Energy dispersive X-ray spectra of 2503 grade silicon milled for 1 hr. The solid line is a least squares fit to the data.

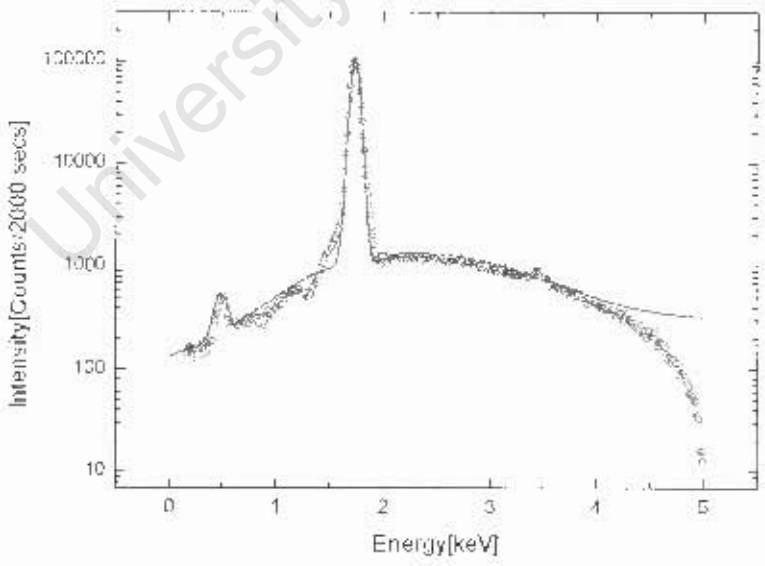

Figure A.14: Energy dispersive X ray spectra of 2503 grade silicon milled for 2 hrs. The solid line is a least squares fit to the data.

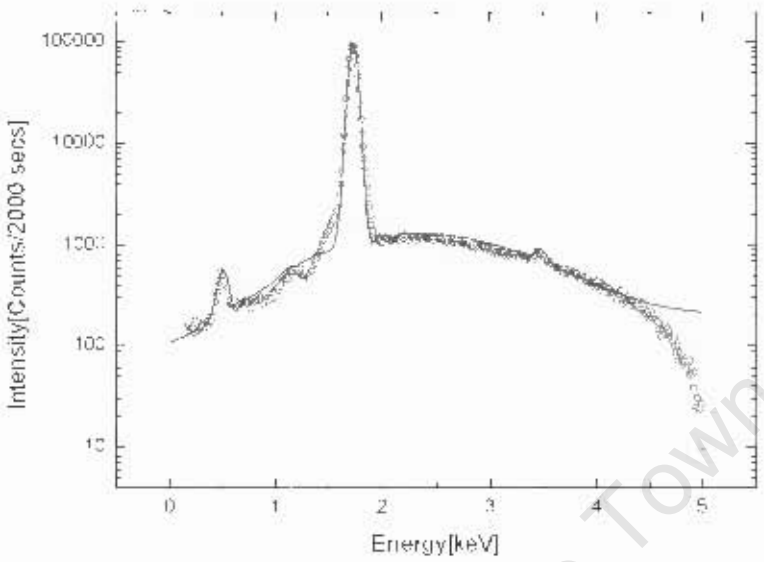

Figure A.15: Energy dispersive X-ray spectra of 2503 grade silicon milled for 3 hrs. The solid line is a least squares fit to the data.

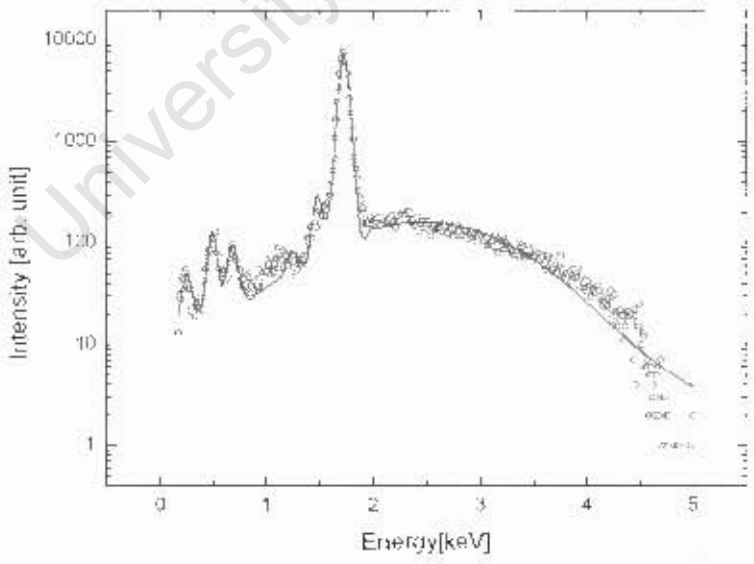

Figure A.16: Energy dispersive X-ray spectra of steel ball milled silicon. The solid line is a least squares fit to the data.

A.2.2 XPS plots for high energy and low energy milled Si.

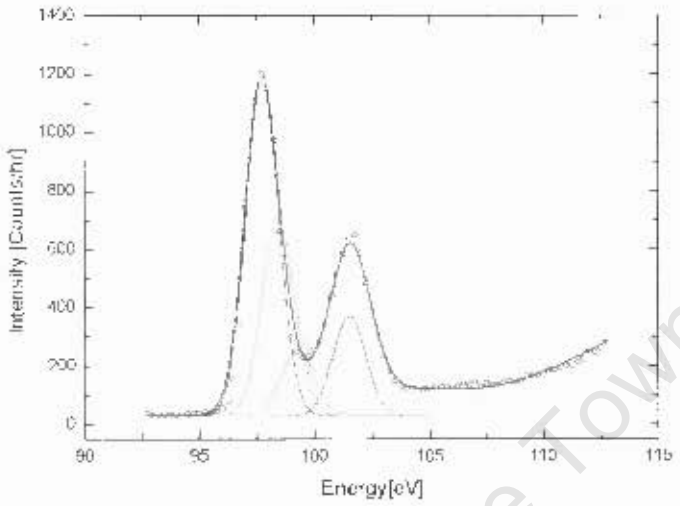

Figure A.17: Si 2*p* photoelectron peaks for silicon milled for 30 mins by high energy milling. The solid line is a fit to the data.

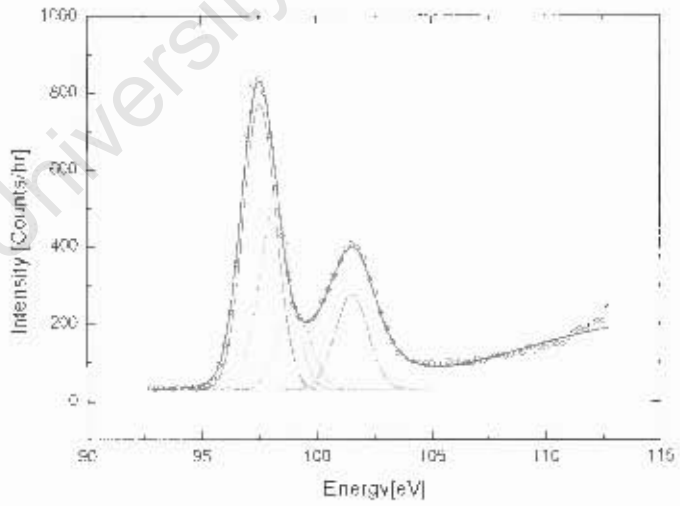

Figure A.18: Si 2*p* photoelectron peaks for silicon milled for 1 hr by high energy milling. The solid line is a fit to the data.

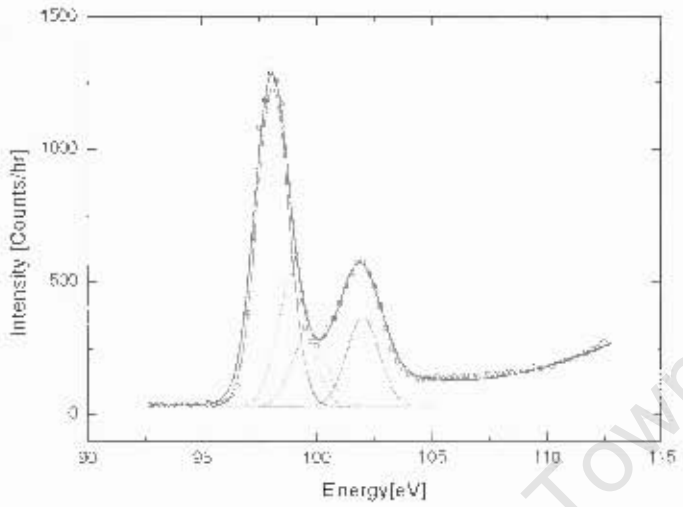

Figure A.19: Si 2p photoelectron peaks for silicon milled for 2 hrs by high energy milling. The solid line is a fit to the data.

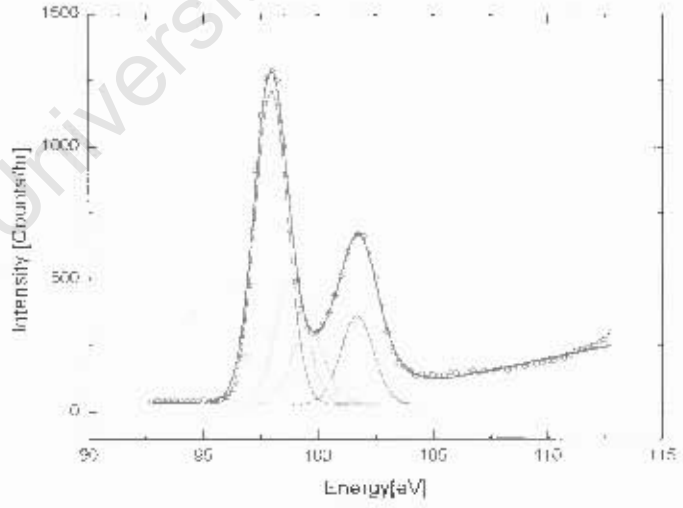

Figure A.20: Si 2p photoelectron peaks for silicon milled for 3 hrs by high energy milling. The solid line is a fit to the data.